Chapter 4
Mechanical Design: Flexure-Based Nanopositioners

The dynamic performance of a nanopositioning system depends on its mechanical resonance frequency, damping, the type of controller used, sensor bandwidth, and associated data acquisition hardware. Recently, speed has become a critical issue in many nanopositioning applications, such as video-rate AFM and high-throughput nanomanufacturing. One of the key limitations in speed is the system's mechanical resonance. As a result, recent efforts have focused on designing the mechanical system to have the highest possible mechanical resonance while maintaining acceptable range of motion. In this chapter, an overview of mechanical design is presented, where the emphasis is on flexure-guided nanopositioning stages for high-speed nanopositioning. The discussions will focus on systems driven by piezoelectric actuators such as plate-stacks, which are readily available from a number of commercial suppliers.

4.1 Introduction

The performance of a nanopositioning system is often dictated by the quality of the mechanical design (Yong et al. 2012). In fact, good mechanical design will minimize most position errors and improve overall accuracy. Poor mechanical design, on the other hand, can lead to more errors than the issues associated with the electronics and other components. Additionally, with good mechanical control systems can be designed to take advantages of the physical characteristics of the positioning stage. The important factors to consider for good mechanical design include: stability of shape and dimension of the positioning stage as a function of temperature; mechanical stiffness; and strength, although strength may not matter in most cases and thus will not be discussed. Cost and manufacturability are also two important factors, especially when it comes to commercialization.

In terms of speed, high mechanical resonance, that is a *stiff* mechanical design, is desired. Traditional nanopositioning designs employ relatively *flexible* piezoactuators and flexure-based mechanisms. In these designs, the lowest mechanical

A. J. Fleming and K. K. Leang, *Design, Modeling and Control of Nanopositioning Systems*, Advances in Industrial Control,
DOI: 10.1007/978-3-319-06617-2_4, © Springer International Publishing Switzerland 2014

resonance is typically less than 1 kHz for a lateral travel range of 10–100 μm. The first mechanical resonance is one of the major limiting factors in speed (Ando et al. 2002; Schitter et al. 2007). Command signals such as triangle waves at 1/10 to 1/100th the first mechanical resonance can excite dynamics that cause significant output oscillation and distortion. A positioning stage's resonance is related to its effective mass, m_{eff}, and stiffness, k_{eff}. Although the effective mass can be reduced to achieve the same effect, due to robustness issues this is not a recommended approach. In particular, the design must be able to accommodate variations in the mass of a sample tray, for example, without significant affect on the mechanical resonance. In designs involving a mechanical amplification factor A_f, the stiffness k_{eff} is given by

$$k_{\text{eff}} = \frac{k_p}{A_f^2}, \tag{4.1}$$

where k_p is the stiffness of the piezoactuator. Reasonable k_{eff} is achieve when A_f is less than five (Hicks et al. 1997).

High-speed nanopositioning is needed in many applications, including video-rate SPM. For instance, the dynamic behavior of micro- and nano-scale processes, such as the movement of biological cells, DNA, and molecules, occur at time scales much faster than the scanning capabilities of conventional SPMs, for example an AFM. Therefore, AFMs capable of high-speed operation are required to observe these processes in real-time (Guthold et al. 1999). High-throughput, probe-based nanomanufacturing is also another area where high-speed positioning of the probe tip is needed. Primarily a serial technique, the total process time of probe-based fabrication is proportional to the number of desired features for a given linear scan rate (Snow et al. 1997). In this respect, a high-throughput positioning stage can drastically reduce manufacturing time.

The mechanical design process first begins by considering the environment in which the stage will be operated. To illustrate the design process, the steps taken to design an example serial-kinematic high-speed multiaxis nanopositioner is presented.

4.2 Operating Environment

At the macroscopic level, small changes in the surrounding environment, such as temperature, humidity, and floor motion, usually go undetected. However, at the micron to nanoscale, the effects may be significant. Micro- and nanopositioning stages can be found in many environments, including research laboratories, ultra-high vacuum chambers, precision machine shops, and environmental scanning electron microscopes (Muller et al. 2007; Samara-Ratna et al. 2007). Certain locations may be well-controlled in terms of temperature, humidity, and external mechanical vibrations. In such areas, there is minimal concern that variations in the environmental conditions

will cause a deterioration in the operating performance of the stage. Instead, performance degradation will likely to occur due to mechanical fatigue and thermal issues, the former being a slow process. For example, one major concern is the self-heating of the piezoelectric actuator at high operating frequencies. The high temperature can affect the repeatability, precision, and life of the stage. Thermally induced stress can cause mechanical failure in flexure mechanisms, joints, and glue layers. The heat generation in a piezoelectric material is attributed to hysteretic losses in the material (Devos et al. 2008). An estimate of the thermal active power, P_a, generated in the actuator due to a sinusoidal input signal is given by Physik Instrumente (2009)

$$P_a \approx \frac{\pi}{4} \tan(\delta) f C V_{pp}^2, \tag{4.2}$$

where f is the frequency of the input signal (in Hz), C is actuator's nominal capacitance, V_{pp} is the peak-to-peak voltage of the input signal, and $\tan(\delta)$ is the dielectric (loss) factor. Under large signal conditions, as much as 12 % of the electrical power used to drive the actuator is converted to heat. The generated heat can limit the actuator's performance, and if not properly isolated, nearby samples and components can be affected. Therefore, best cooling practices should be employed for the actuator and drive electronics. Furthermore, it has been shown that the optimal operating frequency for minimal heat dissipation is close to the resonance frequency for standard piezoelectric materials (Devos et al. 2008).

But for environments where significant fluctuations in operating conditions exist, special considerations should be taken during the design process. For instance, a well-sealed and water-resistant enclosure is recommended for devices, which operate in areas prone to contact with liquids such as coolants, water, oils, and corrosive elements. An enclosure also prevents conductive particles such as fine metal shavings from degrading the piezoceramic and causing short circuits. Stainless steel is commonly used as an enclosure material (Physik Instrumente 2009). In some cases, a protective coating can be sprayed over the actuator and stage assembly to provide additional protection from the environment.

Systems which operate in areas prone to large temperature fluctuations and high temperatures should be closely monitored and protected against. Thermocouple sensors can be used to measure the temperature of critical or nearby components to ensure that excessive heating does not occur. An environment chamber in which the temperature can be closely controlled may be required.

Positioning stages used in areas where a significant level of external mechanical vibration exists should be properly isolated. The lack of isolation will allow the transmission of mechanical disturbances, which can excite the resonances of the positioning system, therefore affecting accuracy. The frequency of vibration of a tall building due to wind is on the order of 1 to 50 Hz. Nearby machinery and equipment can vibrate up to several hundred Hertz. A survey of the vibration level of the environment should be done to determine whether specialized foundations and vibration isolation platforms are required. Additionally, acoustic vibrations in the air should also be considered and protected against. A simple acoustic chamber can

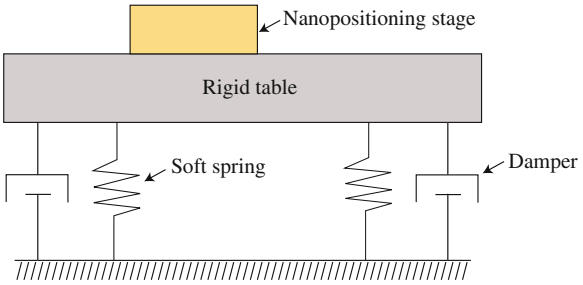

Fig. 4.1 Vibration isolation table consisting of a rigid table supported by soft springs and dampers

be constructed using readily available acoustic foam with a sufficiently high noise reduction coefficient (NRC).

The goal of using a vibration isolation platform is to minimize the effect of relative motion between any two or more components. Building vibration and vibration from other sources such as a fan motor in a nearby desktop computer can transmit through workbench mounting points to the positioning stage. The isolation table basically consists of a rigid table supported by relatively soft spring legs with damping as shown in Fig. 4.1. The *quality* of a vibration isolation platform (optic table) that is schematically depicted in Fig. 4.1 is quantified in terms of its compliance $\mathcal{C}$, the ratio of the excited vibrational amplitude x to the magnitude of the forcing vibration F. The lower the compliance, the better the table upon which the nanopositioning stage rests. In other words, the table should have zero or minimal response due to an applied force or vibration. An ideal table is a rigid body, which does not resonate, and it exhibits a compliance given by

$$\mathcal{C} \triangleq \frac{x}{F} = \frac{1}{f^2}, \tag{4.3}$$

where f is the frequency. Therefore, the quality of any table should be compared to the compliance of the ideal case (4.3). To understand the effects of table mass, leg stiffness, and damping, consider the following one degree-of-freedom compliance relationship for the vibration table shown in Fig. 4.1,

$$\mathcal{C} = \frac{1/k}{\sqrt{(1 - f^2/f_n^2) + (2\zeta f/fn)^2}}, \tag{4.4}$$

where k is the stiffness, ζ is the damping coefficient, and f_n is the natural resonance frequency. At low frequencies the compliance is determined by the stiffness of the table, therefore, the higher the stiffness the lower the compliance. At resonance, however, the compliance is dominated by the amount of damping, thus damping is critical in reducing the transmission of vibration from the environment to the table near the table's resonance. Finally, the mass of the table only makes a significant

contribution at high frequencies. Ideally, the resonance frequency of the table itself should be made as low as possible to avoid excitation caused by building vibration.

4.3 Methods for Actuation

Aside from using piezoelectric actuators for creating displacement, other possible candidates for include electrostrictive and magnetostrictive actuators. Like piezoelectric materials, electrostrictives (Damjanovic and Newnham 1992) can convert electrical to mechanical energy and vice versa. The strain to voltage relationship for an electrostrictive actuator is governed by

$$\epsilon = cV^2, \tag{4.5}$$

where c is a constant. The achievable strain can be as much as 0.15 %, and one major advantage is they exhibit much lower hysteresis compared to standard PZT. However, optimum performance can only be achieved over a narrow electric field and temperature range.

Magnetostrictive materials (Stillesjo et al. 1998; Tan and Baras 2004), which convert magnetic to mechanical energy, offer relatively linear behavior within the range of 0.1 % strain. The governing equations for these materials are similar to those for piezoelectrics. These materials have been applied to the development of micropositioning systems (Tsodikov and Rakhovsky 1998).

Shape memory alloy (SMA), for example nickel-titanium, is a *active material* whereby a change in temperature causes a change in the atomic crystal structure of the alloy. As a result, the material undergoes shape change with achievable strain as high as 8 % when the material transforms between the martensite phase (monoclinic at low temperature) and the austenite phase (cubic at high temperature) (Waram 1993). This unique behavior can be exploited to create SMA-based actuators (or positioners), and compared to piezoelectric actuators, SMAs offer relatively large strain and high strength-to-weight ratio (e.g., recovery stress $>$ 500 MPa). Unfortunately, their slow response times and significant hysteresis behavior limit their application in high speed nanopositioning.

Compliant microelectromechanical systems (MEMS) for microscale positioning can be achieved using electrostatic, thermal, piezoelectric, pneumatic, as well as magnetostrictive and electromagnetic actuation (Liu 2006). Such devices are created using standard or specialized MEMS fabrication techniques. A graphical performance chart has been developed to provide a quantitative comparison of MEMS-based actuators in terms of maximum force, displacement capability, resolution, and natural frequency (Bell et al. 2005). Additionally, a detailed review of actuators for micro- and nano-positioners can be found in Hubbard et al. (2006), Sahu et al. (2010). Performance of the actuators is delineated based on range, resolution, footprint, output force, speed of response (bandwidth), and electrical drive considerations. It is worth noting that electrothermal and electrostatic actuators are the most widely used

actuators for nanoscale applications. This is because of their straightforward integration with standard MEMS-based fabrication processes, relatively small footprint (<1 mm^2) and design simplicity. More specifically, electrothermal actuators operate on the principle of Joule heating and differential thermal expansion (Liu 2006; Bechtold et al. 2005). In particular, an electrical closed-loop is formed by designing the actuating mechanism to consist of a 'hot' and 'cold' arm. The difference in the heating of each arm induces strain, and thus mechanical deformation. Typically, electrothermal actuators are suitable for large deflection (up to 20 μm), with output force in the micro- to milli-Newton range (10 μN to 10 mN), and operating voltage well below 15 V. These actuators exhibit the smallest footprints (<1 mm^2) making them suitable for a wide variety of nanoscale applications. However, the high temperature (200–600 °C) may be undesirable for certain temperature sensitive applications. An extensive review of electrothermal actuators can be found in (Geisberger and Sarkar 2006). MEMS-based electrostatic actuators operate on the principle of Coulomb attraction due to application of a bias voltage between two plates (moving and fixed) (Hubbard et al. 2006; Geisberger and Sarkar 2006). For the simplest parallel-plate configuration, the capacitance C gives a measure of the stored energy, which is a function of the plate area A, permittivity of the medium ϵ_o, and distance between the plates d. In general, the output force is a nonlinear function of the gap between the plates. The operating voltage ranges from 20–100 V. Electrostatic microactuators provide higher positioning resolution (<1.5 nm) and faster response (micro-second range) as compared to electrothermal actuators. Because of their straightforward fabrication, small footprint (≈ 1 mm^2), and low power consumption they find potential use at the nanoscale. However, they are not preferable for applications such as in-situ manipulation in electron microscopes as electric fields due to high voltage may interfere with the imaging electron beam.

4.4 Flexure Hinges

4.4.1 Introduction

Although piezoactuators are capable of sub-nanometer positioning resolution, they provide limited travel range. A modest 10-mm long piezo-stack actuator (Noliac SCMA-P7) at full drive voltage of 200 V extends a maximum of 11 μm (unconstrained). Larger displacements can be achieved with longer actuators or mechanical amplifiers. However, it is pointed out that these options come at a cost of lower mechanical bandwidth (that is, resonance frequency) due to the reduction of effective stiffness. In fact, the first resonance frequency is inversely proportional to an actuator's maximum stroke. To illustrate, consider a fixed-free plate-stack piezoactuator with constant rectangular cross-section. The extension of the actuator along its length (longitudinal displacement) is given by

Fig. 4.2 A gripper with four flexure hinges and four rigid links

$$\delta \approx d_{31} L U, \tag{4.6}$$

where d_{31} is the strain coefficient perpendicular to the polarization direction, L is the length of the actuator, and U is the electric field. From vibrations, the frequency of the first longitudinal mode of the stack actuator can be expressed as Inman (2001)

$$f = \frac{\pi}{L}\sqrt{\frac{E}{\rho}}, \tag{4.7}$$

where E is the elastic modulus and ρ is the density. By eliminating the dependence on the actuator length L in Eq. (4.7) using (4.6), the frequency of the first longitudinal mode is

$$f = \frac{\pi d_{33} U}{\delta_z}\sqrt{\frac{E}{\rho}} \propto \frac{1}{\delta_z}. \tag{4.8}$$

Therefore, the first resonance frequency is inversely proportional to the actuator's maximum displacement δ. Higher bandwidth is achieved by using more compact piezoactuators, but the achievable travel range is reduced.

Flexure hinges are commonly employed in the design of effective mechanical amplifiers for macro as well as MEMS-based devices. Figure 4.2 shows an application of flexure hinges. The gripper mechanism consists of four flexures connecting four rigid links. The use of flexure hinges over traditional rotational joints enables the gripper to be easily manufactured as one part. For nanopositioning, as illustrated in Fig. 4.3a1,a2, for a given actuator stroke δ, a flexure-based mechanical amplifier provides a scaled output of $a\delta$, where a is primarily a function of the geometry of the mechanical amplifier. Flexure hinges are also commonly employed to guide the motion of sample stages to minimize parasitic motion, as well as to increase the stiffness of an actuator along off-axis or out-of-plane directions to improve mechanical resonances. Figure 4.3b1,b2 show an example of a single-axis positioning stage for displacing a mass m. The flexure hinges, one on each side of the mass, serve to guide the motion of the mass along a straight path.

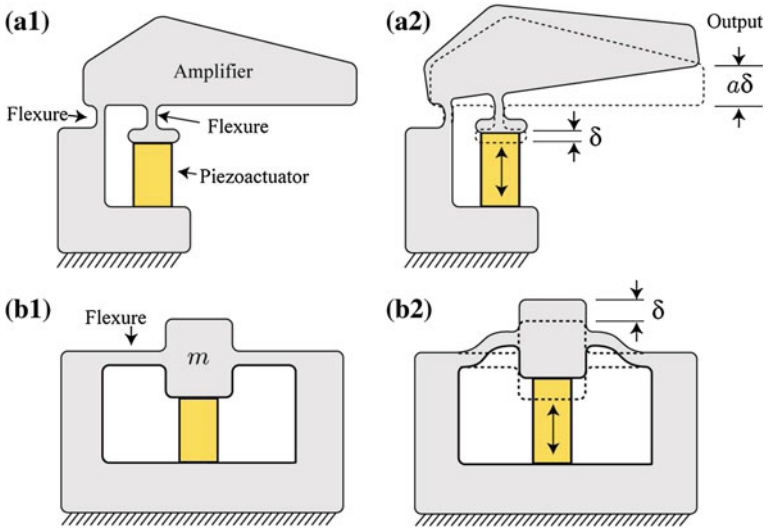

Fig. 4.3 Application of flexure hinges: **a1** and **a2** mechanical amplifier; **b1** and **b2** motion guiding to minimize runout

As indicated by the examples in Fig. 4.3, a flexure hinge is simply a thin elastic member that connects two rigid bodies and provides limited relative rotational motion through bending or flexing. The major distinction between a classical mechanical joint, such as a rotational bearing, and a flexure hinge is that the center of rotation for the two connected members in the former are collocated, whereas for the flexure hinge the rotation is noncollocated. Interested readers will find detailed discussions on flexure design and compliant mechanisms in Smith (2000), Howell (2001), Lobontiu (2003). For nanopositioning systems, flexure hinges are far more compact compared to traditional mechanical hinges. They are invaluable because there is no friction loss, need for lubrication, or hysteresis effects.

4.4.2 Types of Flexures

Flexure hinges can be designed for one to multiple degrees-of-freedom motion as illustrated in Fig. 4.4. For example a single axis flexure hinge (Fig. 4.4a) is used for planar motion, where as two- and multi-axis flexure hinges (Fig. 4.4b, c) are ideally suited for three-dimensional motion. Standard milling and electrical discharge machining are used to create the one and two degrees-of-freedom flexures, where as a turning operation is used to create the multiaxis flexure hinge shown in Fig. 4.4c.

Commonly used flexure hinge designs are shown in Fig. 4.5. The corner-filleted design offers more evenly distributed stresses compared to the basic design of Fig. 4.5a.

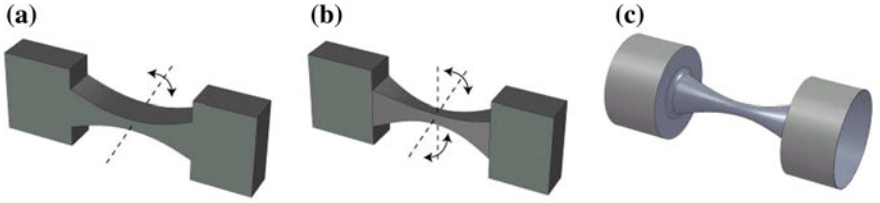

Fig. 4.4 Flexure degrees of freedom: **a** one, **b** two, and **c** multiple degrees-of-freedom

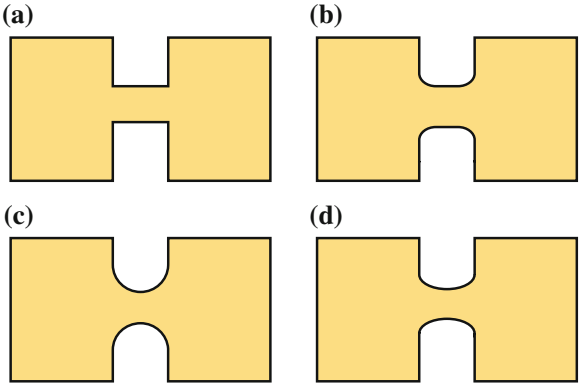

Fig. 4.5 Different types of flexure hinges: **a** basic, **b** filleted, **c** circular, and **d** elliptical

The flexure geometries shown in Fig. 4.4 are often of a monolithic design; that is, milled, turned, or specially machined from a solid block of material. However, flexure hinges can be made by assembling thin members with rigid members using fasteners or through bonding. Examples of multiaxis nanopositioning stages made from these two types of flexures are shown in Fig. 4.6. The main advantage of making a flexure from individual parts is it can be fabricated with standard milling and turning processes. The disadvantage of assembled flexures is performance. Because fasteners and adhesives are used, inconsistencies in the assembly process and boundary conditions can have a drastic effect on the flexures static and dynamic performance. On the other hand, monolithic designs offer more predictable and repeatable performance. However, monolithic designs, especially for flexure with extremely thin dimensions, may require specialized machining processes such as wire electrical discharge machining or MEMS fabrication techniques.

4.4.3 Flexure Hinge Compliance Equations

Flexure hinges are frequently designed to operate over small displacements and angles of rotation. For homogenous linear elastic and isotropic materials, the closed-form solution for the deformation of a flexure hinge can be derived using, for example,

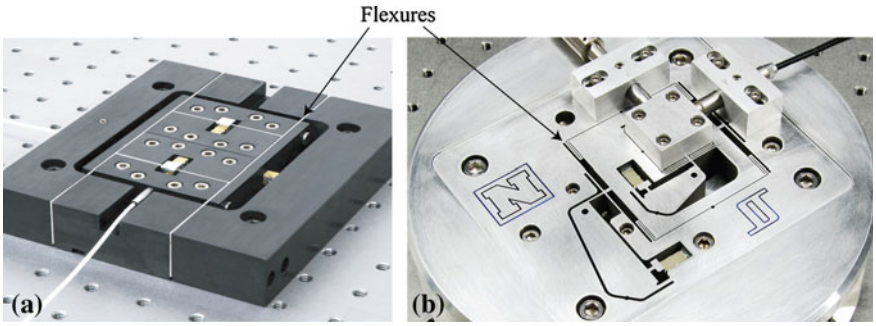

Fig. 4.6 Examples of flexures made by **a** assembling thin members with rigid blocks (Leang and Fleming 2009) and **b** monolithic design fabricated by wire electrical discharge machining

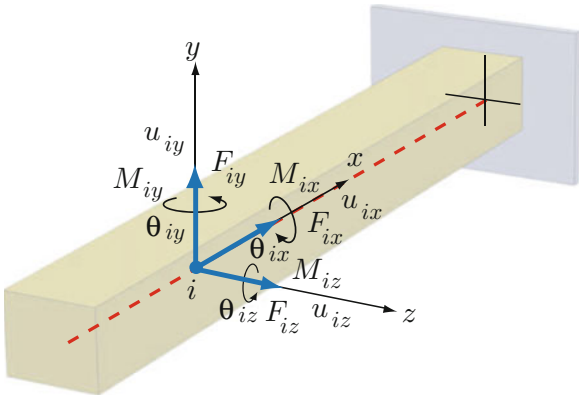

Fig. 4.7 Generic flexure member

Castigliano's displacement (second) theorem (Lobontiu 2003). Consider as an example, the generic flexure member, which is shown as a long slender beam, in Fig. 4.7.

Castigliano's displacement theorem enables the calculation of deformations (or rotations) of elastic bodies at a specific point i under external loading, moments, or support reactions acting at that location. The linear and angular deformations at location i due to force F_i and moment M_i are

$$u_i = \frac{\partial E_\epsilon}{\partial F_i}, \tag{4.9}$$

$$\theta_i = \frac{\partial E_\epsilon}{\partial M_i}, \tag{4.10}$$

where E_ϵ is the strain energy. In the event that a deformation at location i is sought where there are no loads or reactions applied at that location, fictitious loads, $\hat{F}_i$ and $\hat{M}_i$, are used and the deformations are determined using Eqs. (4.9) and (4.10).

The example long slender beam in Fig. 4.7 is subjected to bending, shearing, axial load, and torsion. Therefore, the strain energy can be expressed as Lobontiu (2003)

$$E_\epsilon = E_{\epsilon,\text{ bending}} + E_{\epsilon,\text{ shearing}} + E_{\epsilon,\text{ axial}} + E_{\epsilon,\text{ torsion}}. \tag{4.11}$$

Specifically,

$$\begin{aligned} E_{\epsilon,\text{ bending}} &= E_{\epsilon,\text{ bending},y} + E_{\epsilon,\text{ bending},z}, \\ &= \int_L \frac{M_y^2}{2EI_y}\,\mathrm{d}s + \int_L \frac{M_z^2}{2EI_z}\,\mathrm{d}s; \end{aligned} \tag{4.12}$$

$$\begin{aligned} E_{\epsilon,\text{ shearing}} &= E_{\epsilon,\text{ shearing},y} + E_{\epsilon,\text{ shearing},z}, \\ &= \int_L \frac{\alpha V_y^2}{2GA}\,\mathrm{d}s + \int_L \frac{\alpha V_z^2}{2GA}\,\mathrm{d}s; \end{aligned} \tag{4.13}$$

$$\begin{aligned} E_{\epsilon,\text{ axial}} &= E_{\epsilon,\text{ axial},x}, \\ &= \int_L \frac{P_x^2}{2EA}\,\mathrm{d}s; \end{aligned} \tag{4.14}$$

$$\begin{aligned} E_{\epsilon,\text{ torsion}} &= E_{\epsilon,\text{ torsion},x}, \\ &= \int_L \frac{M_x^2}{2GJ}\,\mathrm{d}s; \end{aligned} \tag{4.15}$$

where α is a constant based on the cross-section. Equations (4.9–4.15) can be combined into the following matrix form

$$\delta_i = \mathcal{C}_i \mathbf{P}_i, \tag{4.16}$$

where $\delta_i = [u_i\ \theta_i]^T$, $\mathcal{C}_i$ is the compliance (flexibility) matrix, and $\mathbf{P}_i$ represents all the loads and moments acting at point i.

Closed-form capacity and precision for rotation solutions for many flexure hinge geometries can be found in Lobontiu (2003). In the following, a brief summary of the results for the capacity for rotation of single-axis flexure hinges with constant width and vertical profiles as shown in Fig. 4.8 are presented for convenience. These flexures are ideally suited for planar motion, and they are used extensively in the design of parallel (Schitter et al. 2007) and serial-kinematics (Leang and Fleming 2009) nanopositioning stages.

First, it is the assumed that the flexure is relatively long compared to the dimensions of its cross-section. For shorter flexure design where shearing effects must be taken into account, see results in Lobontiu (2003). Let L denote the length of the flexure and $t(x)$ be its thickness as a function of the location x. The minimum thickness of the flexure over L is given by t.

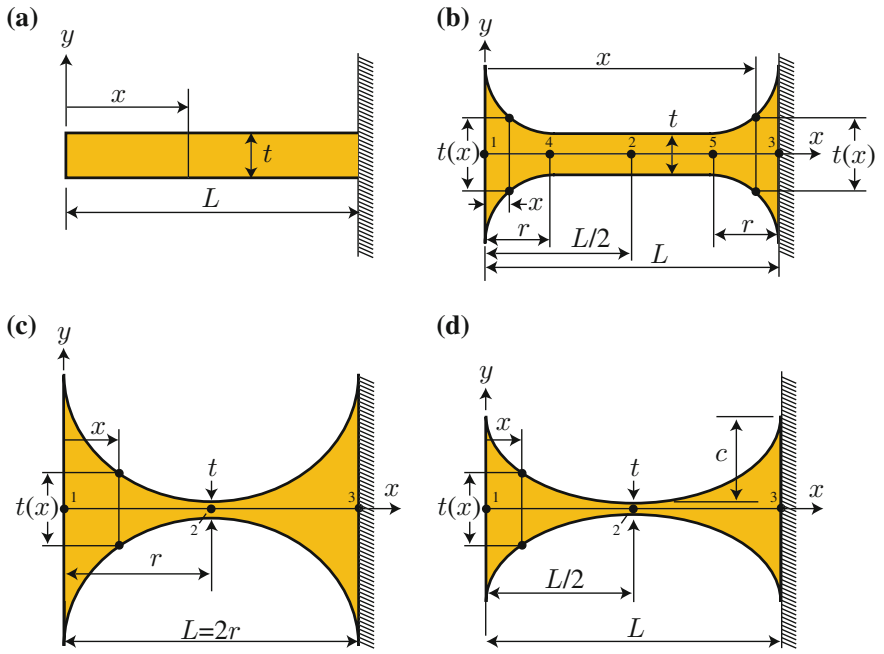

Fig. 4.8 Commonly used flexure hinges and their dimensions: **a** basic, **b** corner-filleted, **c** circular, and **d** ellipse

In these types of flexures, the loading at the free end (location 1) has the following six components:

- two bending moments, M_{1y} and M_{1z};
- two shearing forces, F_{1y} and F_{1z};
- one axial load, F_{1x}; and
- one torsional moment, M_{1x}.

The in-plane components, M_{1z}, F_{1y}, and F_{1x} are the most significant. The out-of-plane components M_{1y}, F_{1z}, and M_{1x} are generally lower in magnitude and appear due to manufacturing and assembly issues. The torsional component can be neglected. Taking these into account, the deformation equation (4.9) can be written as

$$\begin{bmatrix} \mathbf{u}_1^{ip} \\ \mathbf{u}_1^{op} \end{bmatrix} = \begin{bmatrix} \mathcal{C}_1^{ip} & 0 \\ 0 & \mathcal{C}_1^{op} \end{bmatrix} \begin{bmatrix} \mathbf{P}_1^{ip} \\ \mathbf{P}_1^{op} \end{bmatrix}, \tag{4.17}$$

where the displacement and load vectors $\mathbf{u}$ and $\mathbf{P}$, respectively, have been divided into in-plane (superscript ip) and out-of-plane (superscript op) subvectors. The subvectors are

$$\mathbf{u}_1^{ip} = \begin{bmatrix} u_{1x} \\ u_{1y} \\ \theta_{1z} \end{bmatrix}; \quad \mathbf{u}_1^{op} = \begin{bmatrix} u_{1z} \\ \theta_{1y} \end{bmatrix}; \quad \mathbf{P}_1^{ip} = \begin{bmatrix} F_{1x} \\ F_{1y} \\ M_{1z} \end{bmatrix}; \quad \mathbf{P}_1^{op} = \begin{bmatrix} F_{1z} \\ M_{1y} \end{bmatrix}. \tag{4.18}$$

The in- and out-of-plane submatrices are

$$\mathcal{C}_1^{ip} = \begin{bmatrix} C_{1,x-F_x} & 0 & 0 \\ 0 & C_{1,y-F_y} & C_{1,y-M_z} \\ 0 & C_{1,\theta_z-F_y} & C_{1,\theta_z-M_z} \end{bmatrix}; \quad \mathcal{C}_1^{op} = \begin{bmatrix} \mathcal{C}_{1,z-F_z} & \mathcal{C}_{1,z-M_y} \\ \mathcal{C}_{1,\theta_y-F_z} & \mathcal{C}_{1,\theta_y-M_y} \end{bmatrix}, \tag{4.19}$$

where $C_{1,y-M_z} = C_{1,\theta_z-F_y}$ and $C_{1,z-M_y} = C_{1,\theta_y-F_z}$. The in-plane compliance equations are

$$\begin{aligned} C_{1,x-F_x} &= \frac{1}{Ew} I_1; \quad C_{1,y-F_y} = \frac{12}{Ew} I_1 2; \\ C_{1,y-M_x} &= \frac{1}{Ew} I_3; \quad C_{1,\theta_z-M_z} = \frac{12}{Ew} I_4. \end{aligned} \tag{4.20}$$

The out-of-plane compliance equations are

$$\begin{aligned} C_{1,z-F_z} &= \frac{12}{Ew^3} I_5; \quad C_{1,z-M_y} = \frac{12}{Ew^3} I_6; \\ C_{1,\theta_y-M_y} &= \frac{12}{Ew^3} I_1 = \frac{12}{w^2} C_{1,x-F_x}. \end{aligned} \tag{4.21}$$

And finally, the integrals above are

$$\begin{aligned} I_1 &= \int_0^L \frac{1}{t(x)}\, \mathrm{d}x; \quad I_2 = \int_0^L \frac{x^2}{t^3(x)}\, \mathrm{d}x; \quad I_3 = \int_0^L \frac{x}{t^3(x)}\, \mathrm{d}x; \\ I_4 &= \int_0^L \frac{1}{t^3(x)}\, \mathrm{d}x; \quad I_5 = \int_0^L \frac{x^2}{t(x)}\, \mathrm{d}x; \quad I_6 = \int_0^L \frac{x}{t(x)}\, \mathrm{d}x. \end{aligned} \tag{4.22}$$

For a constant rectangular cross-section flexure hinge as shown in Fig. 4.8a, where the thickness is $t(x) = t$ for $0 \leq x \leq L$, the in-plane compliances are founded by solving the integrals in Eq. (4.22) and substituting the results into Eq. (4.20). The final results are

$$\begin{aligned} \mathcal{C}_{1,x-F_x} &= \frac{L}{Ewt}; \quad \mathcal{C}_{1,y-F_y} = \frac{4L^3}{Ewt^3}; \\ \mathcal{C}_{1,y-M_z} &= \frac{6L^2}{Ewt^3}; \quad \mathcal{C}_{1,\theta_z-M_z} = \frac{12L}{Ewt^3}; \\ \mathcal{C}_{1,z-F_z} &= \frac{4L^3}{Ew^3t}; \quad \mathcal{C}_{1,z-M_y} = \frac{6L^2}{Ew^3t}; \end{aligned}$$

$$\mathcal{C}_{1,\theta_y-M_y} = \frac{12L^3}{Ew^3t}. \tag{4.23}$$

For a corner-filleted flexure hinge as shown in Fig. 4.8b, where the thickness is

$$t(x) = \begin{cases} t + 2\left[r - \sqrt{x(2r-x)}\right], & x \in [0, r] \\ t, \quad x \in [r, L-r] \\ t + 2\{r - \sqrt{(L-x)[2r-(L-x)]}\}, & x \in [L-r, r], \end{cases} \tag{4.24}$$

the in-plane compliances are

$$\begin{aligned}
\mathcal{C}_{1,x-F_x} &= \frac{1}{Ew}\left[\frac{L-2r}{t} + \frac{2(2r+t)}{\sqrt{t(4r+t)}}\arctan\sqrt{1+\frac{4r}{t}} - \frac{\pi}{2}\right]; \\
\mathcal{C}_{1,y-F_y} &= \frac{3}{Ew}\left\{\frac{4(L-2r)(L^2-Lr+r^2)}{3t^3}\right. \\
&\quad + \frac{\sqrt{t(4r+t)}[-80r^4+24r^3t+8(3+2\pi)r^2t^2]}{4\sqrt{t^5(4r+t)^5}} \\
&\quad + \frac{\sqrt{t(4r+t)}[4(1+2\pi)rt^3+\pi t^4]}{4\sqrt{t^5(4r+t)^5}} \\
&\quad + \frac{(2r+t)^3(6r^2-4rt-t^2)\arctan\sqrt{1+\frac{4r}{t}}}{\sqrt{t^5(4r+t)^5}} \\
&\quad + \frac{-40r^4+8Lr^2(2r-t)+12r^3t+4(3+2\pi)r^2t^2}{2t^2(4r+t)^2} \\
&\quad + \frac{2(l+2\pi)rt^3+\frac{\pi t^4}{2}}{2t^2(4r+t)^2} + \frac{4L^2r(6r^2+4rt+t^2)}{t^2(2r+t)(4r+t)^2} \\
&\quad - \frac{(2r+t)[-24(L-r)^2r^2-8r^3t+14r^2t^2+8rt^3+t^4]}{\sqrt{t^5(4r+t)^5}} \\
&\quad \left.\times \arctan\sqrt{1+\frac{4r}{t}}\right\}; \\
\mathcal{C}_{1,y-M_z} &= -\frac{6L}{Ewt^3(2r+t)(4r+t)^2}\left\{(4r+t)[L(2r_t)(4r+t)^2\right. \\
&\quad - 4r^2(16r^2+13rt+3t^2)] + 12r^2(2r+t)^2\sqrt{t(4r+t)} \\
&\quad \left.\times \arctan\sqrt{1+\frac{4r}{t}}\right\}; \\
\mathcal{C}_{1,\theta_z-M_z} &= \frac{12}{Ewt^3}\left\{L-2r+\frac{2r}{(2r+t)(4r+t)^3}\left[t(4r+t)(6r^2+4rt+t^2)\right.\right. \\
&\quad \left.\left. + 6r(2r+t)^2\sqrt{t(4r+t)}\arctan\sqrt{1+\frac{4r}{t}}\right]\right\}.
\end{aligned} \tag{4.25}$$

The out-of-plane compliances are

$$\mathcal{C}_{1,z-F_z} = \frac{12}{Ew^3}\left\{\frac{(L-2r)(L^2-Lr+r^2)}{3t} + Lr\left[\log\frac{t}{2r+t} - \frac{2(L-2r)}{\sqrt{t(4r+t)}}\right.\right.$$
$$\left.\left.\times\ \arctan\sqrt{1+\frac{4r}{t}}\right]\right\};$$
$$\mathcal{C}_{1,z-M_y} = \frac{6}{Ew^3t}\left\{L(L-2r) + 2r\left[t\log\frac{t}{2r+t} - 2(L-2r)\sqrt{\frac{t}{4r+t}}\right.\right.$$
$$\left.\left.\times\ \arctan\sqrt{1+\frac{4r}{t}}\right]\right\};$$
$$\mathcal{C}_{1,\theta_y-M_y} = \frac{6}{Ew^3t}\left[2L-4r = \pi t + 4(2r+t)\sqrt{\frac{t}{4r+t}}\arctan\sqrt{\frac{t}{4r+t}}\right]. \quad (4.26)$$

For a circular flexure hinge as shown in Fig. 4.8c, where the thickness is $t(x) = t + 2[r - \sqrt{x(2r-x)}]$ for $0 \le x \le L$, the final results for the in-plane compliances are

$$\mathcal{C}_{1,x-F_x} = \frac{1}{Ew}\left[\frac{2(2r+t)}{\sqrt{t(4r+t)}}\arctan\sqrt{1+\frac{4r}{t}-\frac{\pi}{2}}\right];$$
$$\mathcal{C}_{1,y-F_y} = \frac{3}{4Ew(2r+t)}\left\{2(2+\pi)r + \pi t + \frac{8r^3(44r^2+28rt+5t^2)}{t^2(4r+t)}\right.$$
$$+\ (2r+t)\sqrt{t(4r+t)}$$
$$\times\ \frac{-80r^4+24r^3t+8(3+2\pi)r^2t^2+4(1+2\pi)rt^3+\pi t^4}{\sqrt{t^5(4r+t)^5}}$$
$$\left.-\ \frac{8(2r+t)^4(-6r^2+4rt+t^2)}{\sqrt{t^5(4r+t)^5}}\arctan\sqrt{1+\frac{4r}{t}}\right\};$$
$$\mathcal{C}_{1,y-M_z} = \frac{24r^2}{Ewt^3(2r+t)(4r+t)^3}\left[t(4r+t)(6r^2+4rt+t^2)\right.$$
$$\left.+\ 6r(2r+t)^2\sqrt{t(4r+t)}\arctan\sqrt{1+\frac{4r}{t}}\right]$$
$$\mathcal{C}_{1,\theta_z-M_z} = \frac{\mathcal{C}_{1,y-M_z}}{r}. \quad (4.27)$$

The out-of-plane compliances are

$$\mathcal{C}_{1,z-F_z} = \frac{24r^2}{Ew^3}\log\frac{t}{2r+t};\quad \mathcal{C}_{1,z-M_y} = \frac{\mathcal{C}_{1,z-F_z}}{2r};$$
$$\mathcal{C}_{1,\theta_y-M_y} = \frac{6}{Ew^3t}\left[4(2r+t)\sqrt{\frac{t}{4r+t}}\arctan\sqrt{\frac{t}{4r+t}} - \pi t\right]. \tag{4.28}$$

Finally, for an ellipse flexure hinge as shown in Fig. 4.8d, with the thickness given by

$$t(x) = t + 2c\left[1 - \sqrt{1 - \left(1 - \frac{2x}{c}\right)^2}\right], \tag{4.29}$$

where c is a constant, the in-plane compliances are

$$\mathcal{C}_{1,x-F_x} = \frac{1}{4Ewc}\left[\frac{4(2c+t)}{\sqrt{t(4c+t)}}\arctan\sqrt{1+\frac{4c}{t}} - \pi\right];$$
$$\mathcal{C}_{1,y-F_y} = \frac{3L^3}{16Ewt^3c^3(2c+t)(4c+t)^2}\Big\{t[96c^5 + 96c^4t + 8(11+4\pi)c^3t^2$$
$$+ 32(1+\pi)c^2t^3 + 2(2+5\pi)ct^4 + \pi t^5] - 4\sqrt{\frac{t}{4c+t}}(2c+t)^4$$
$$(-6c^2 + 4ct + t^2)\arctan\sqrt{1+\frac{4c}{t}}\Big\};$$
$$\mathcal{C}_{1,y-M_z} = \frac{6L^2}{Ewt^2(2c+t)(8c^2+t^2)}$$
$$\times\left[6c^2 + 4ct + t^2 + \frac{6c(2c+t)^2}{\sqrt{t(4c+t)}}\arctan\sqrt{1+\frac{4c}{t}}\right]. \tag{4.30}$$

The out-of-plane compliances are

$$\mathcal{C}_{1,z-F_z} = \frac{3L^3}{16Ew^3c^3}\left\{2(4-\pi)c^2 + 4(1+\pi)ct + \frac{(2c+t)(-4c^2+4ct+t^2)}{\sqrt{t(4c+t)}}\right.$$
$$\left.\times\left[2\arctan\frac{2c}{\sqrt{t(4c+t)}} - \pi\right]\right\};$$
$$\mathcal{C}_{1,z-M_y} = \frac{3L^2}{2Ew^3c}\left\{\frac{2c+t}{\sqrt{t(4c+t)}}\left[2\arctan\frac{2c}{\sqrt{t(4c+t)}} + \pi\right] - \pi\right\}. \tag{4.31}$$

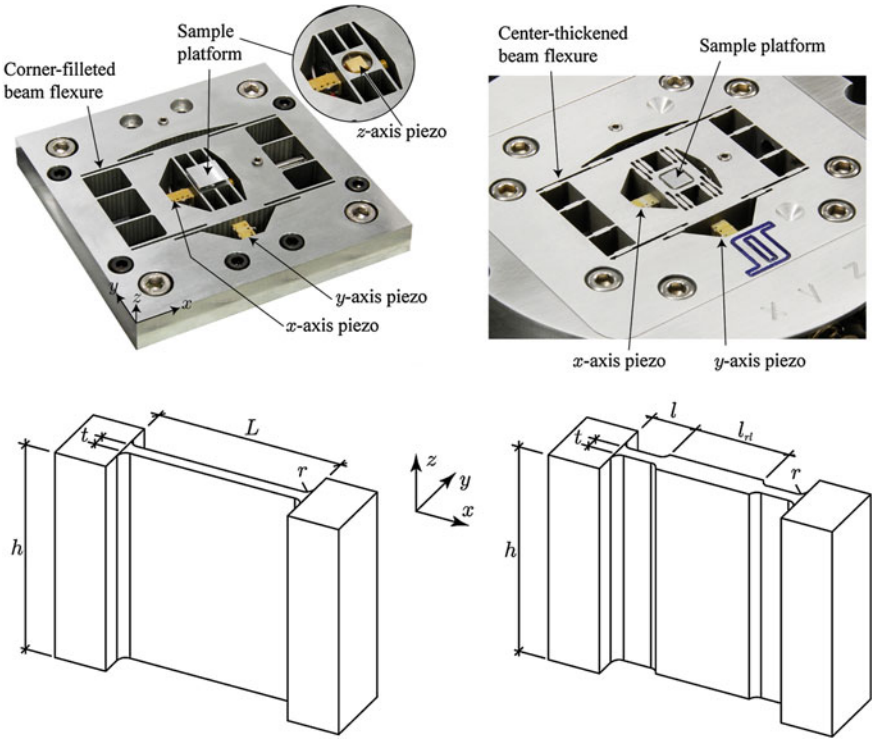

Fig. 4.9 Flexure design for increased out-of-plane stiffness. *Left* conventional corner-filleted beam flexure; and *right* serial-compliant double-hinged flexure with thickened center section

4.4.4 Stiff Out-of-Plane Flexure Designs

The majority of multiaxis nanopositioning stages for applications such as SPMs employ flexures hinges to guide the motion of the sample platform. The main objective is to limit parasitic (i.e., out-of-plane and off-axis) motion so that the stage only moves in the direction of actuation. For scanning at low speed, parasitic motion of the sample platform can be minimized using a simple beam flexure to guide the motion of the platform. As actuation frequencies increase, in- and out-of-plane resonance modes can be excited, thus limiting the positioning speed. However, dominant resonances occurring in the actuation direction are tolerable compared to out-of-plane modes; preferably, if the actuation modes precede the out-of-plane or off-axis modes. To ensure this, flexures should be designed to maximize the out-of-plane stiffness, yet be sufficiently *soft* to avoid affecting the achievable stroke of the actuator. Take the lateral scanning motion for example, where along the x and y-axis the sample platform is connected to simple beam flexures as shown in Fig. 4.9, top and bottom left photograph and sketch. The vertical stiffness of the sample platform can be maximized by (1) increasing the number of flexures in x and y, (2) utilizing shorter

(effective length) flexures, and (3) converting the flexures from constant rectangular cross section beam flexures to a serial-compliant double-hinged flexure with a “rigid" center connecting link as shown in Fig. 4.9 (Kenton and Leang 2012).

It is pointed out that the limiting factor of decreasing the flexure thickness is stress. Shorter thinner beam flexure will have higher stress concentration than a longer thicker beam flexure of equal stiffness. When a corner-filleted beam flexure (Fig. 4.9) is displaced in the vertical direction, the majority of the vertical displacement is caused by shear deformation of the center section. Thus, an effective way to increase the out-of-plane stiffness of a beam flexure is by thickening the center section, effectively converting the beam flexure into a double-hinged serial flexure as shown in Fig. 4.9, top and bottom right photograph and sketch. A serial-compliant flexure is one such that there are more than one flexure or flexure hinge in series with each other separated by a rigid link. By increasing the number of flexures, decreasing the flexure length, and thickening the center section of a beam flexure to create a serial-compliant double-hinged flexure, the effective vertical stiffness can be increased significantly (Kenton and Leang 2012).

4.4.5 Failure Considerations

In the design of flexure hinges for nanopositioning systems, failure due to yield and fatigue must be considered. Failure due to yield occurs when the deformation of the flexure exceeds that of the proportionality limit. Ductile materials are often chosen for flexure design. For ductile and isotropic materials, two most frequently used failure criteria includes the maximum shear stress theory (Tresca) and the maximum energy of deformation theory (von Mises) (Beer and Johnston 1992).

The maximum shear stress criterion is based on the idea that failure in ductile materials is caused by shearing stresses. A given structural component is deemed safe as long as the maximum shear stress $\tau_{\max}$ in the component is less than the shearing stress of the component at yield under a tensile test. Specifically, if the principal stresses σ_a and σ_b have the same sign, the maximum shear stress criterion gives

$$|\sigma_a| < \sigma_y \quad |\sigma_b| < \sigma_y, \tag{4.32}$$

where σ_y is the yield stress of the material. If the principal stresses σ_a and σ_b have opposite signs, the maximum shear stress criterion gives

$$|\sigma_a - \sigma_b| < \sigma_y. \tag{4.33}$$

The maximum energy of deformation criterion states that a given structural component is deemed safe as long as the maximum value of the distortion energy per unit volume of that material is less than the distortion energy per unit volume required to cause yield in a tensile-test specimen of the same material. Under plane stress, the distortion energy per unit volume in an isotropic material is

$$u_d = \frac{1}{6G}(\sigma_a^2 - \sigma_a\sigma_b + \sigma_b^2), \tag{4.34}$$

where G is the modulus of rigidity. A tensile-test specimen when it starts to yield has $\sigma_a = \sigma_y$ and $\sigma_b = 0$, therefore $(u_d)_y = \sigma_y^2/6G$. As a result, as long as $u_d < (u_d)_y$ or

$$\sigma_a^2 - \sigma_a\sigma_b + \sigma_b^2 < \sigma_y^2, \tag{4.35}$$

then the structural component is safe.

Commonly used failure criteria for brittle materials include the maximum normal stress criterion and Mohr's criterion and can be found in Beer and Johnston (1992). One of the most practical approaches uring the design process to ensure that a given flexure is design within the failure tolerances is to employ finite element programs such as ANSYS (Canonsburg, PA, USA) and Solidworks with COSMOSWorks (Concord, MA, USA).

4.4.6 Finite Element Approach for Flexure Design

The finite element analysis (FEA) method is a power numerical technique for solving engineering and mathematical physics problems that include structural analysis, heat transfer, electro-mechanical coupling, fluid flows, and mass transport. It is particularly useful for problems with complicated geometries, materials properties, loadings, and boundary conditions. Popular commercially available programs includes ANSYS (Canonsburg, PA, USA) and Solidworks with COSMOSWorks (Concord, MA, USA). Figure 4.10 shows FEA results that compare the stress distribution between the basic geometry to that of a corner-filleted flexure (Fig. 4.5b). The ability for generating quick and relatively accurate results using FEA software has made it a popular choice for mechanical design. The FEA programs can also be used to estimate frequency response functions for nanopositioning designs, where results can show the effects of cross-couplings and out-of-plane behaviors. Users can expect accuracy of less than 10 % compared to experimentally measured results (see example in Fig. 4.11).

4.5 Material Considerations

4.5.1 Materials for Flexure and Platform Design

A basic nanopositioning stage consists of a rigid frame upon which an actuator rests and pushes off against to displace a mass or flexure member. The material for the frame as well as any required flexure hinges must be carefully selected for optimum

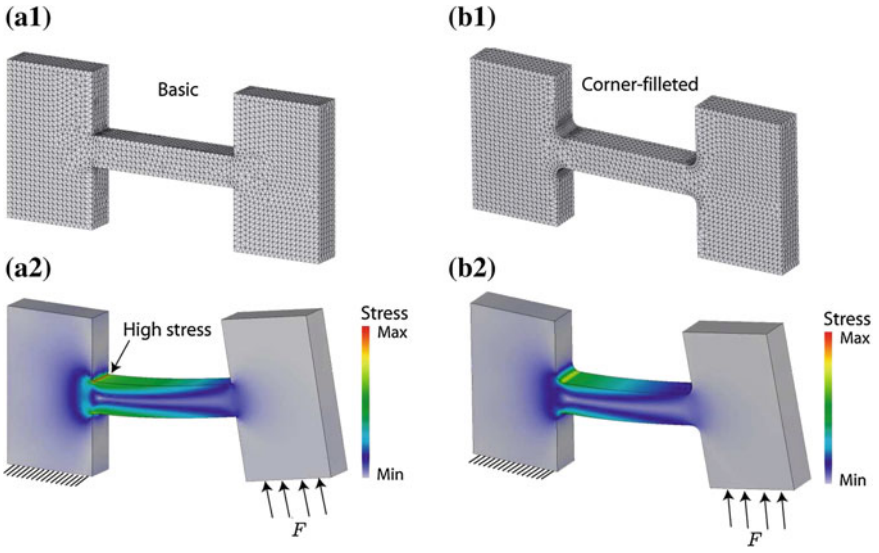

Fig. 4.10 Finite element results comparing the stress distribution between a **a** basic and **b** corner-filleted flexure hinge

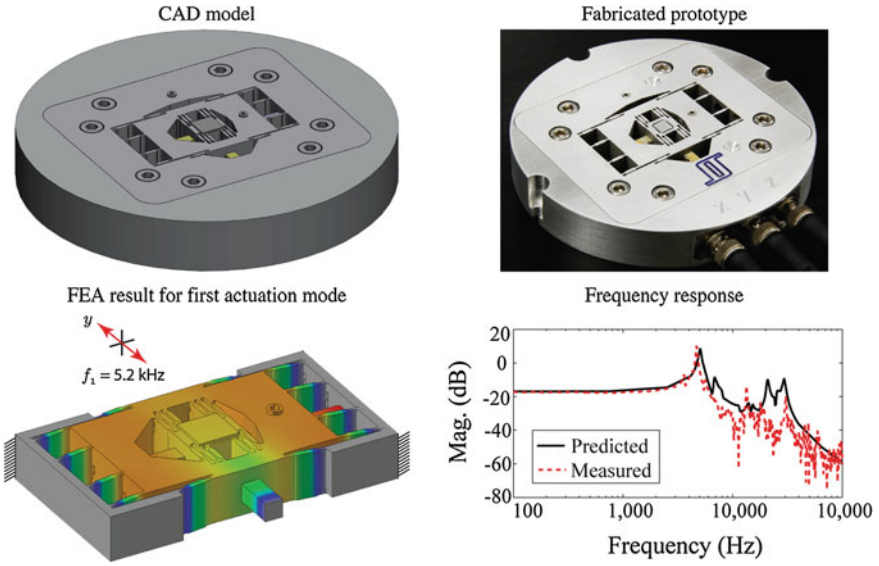

Fig. 4.11 Comparison between FEA predicted and measured dynamic performance

Table 4.1 Properties of various materials

Material	Density (kg/m^3)	Young's Mod. (GPa)	Thermal Cond. (W/m-C)	CTE (10^{-6}/°C)
6061 Aluminum	2710	70	167	23.6
7075 Aluminum	2800	72	130	23.6
Stainless steel	7920	190	16.3	17.3
Titanium	4730	115	15.6	9.5
Invar (Invar 36)	8130	144	13.8	1.6
Super Invar	8137	144	10.5	0.3

static and dynamic performance. Some popular materials are listed in Table 4.1. Aluminum alloys, such as the 7075 grade is the most commonly used due to its machinability and favorable density-to-stiffness ratio. Materials which exhibit extremely low thermal coefficient of expansion include Invar and Super Invar (Schilfgaarde et al. 1999). Stainless steel is often used to create the rigid base due to its high elastic modulus and resistance to corrosion. Likewise, AISA A2 steel, which is easily machinable, has an equivalent elastic modulus to stainless steel following a heat-treating process. The heat-treating process involves heating the material to 850 °C, followed by cooling in the furnace at 10 °C per hour to 650 °C. Finally, the material is cooled freely in air. The other components that require a high stiffness to density ratio, such as the flexure hinges and sample platforms, are constructed from aluminum.

4.5.2 Thermal Stability of Materials

Thermal expansion is the dimensional change of a material due to a change in temperature, and it is generally inversely proportional to the melting point of a material. The effect can severely limit the precision, repeatability, and overall performance of a nanopositioning system, such as causing temperature-dependent drift in motion and thermal stresses which ultimately lead to cracking, warping, or loosening of components.

The change in length (from l_0 to l_f) for a solid material for a given change in temperature (from T_0 to T_f) is given by

$$\frac{l_f - l_0}{l_0} = \alpha(T_f - T_0), \tag{4.36}$$

where α is the linear thermal coefficient of thermal expansion and has units of $(°C)^{-1}$ or K^{-1}. For nanometer motion, thermal effects can not be ignored. Careful material selection and design are effective methods for minimizing thermal effects. Table 4.1 lists the mechanical and thermal properties of commonly-used materials for the design of nanopositioning stages. For example, the coefficient of thermal expansion (CTE) for aluminum is 23×10^{-6} /°C, while for Super Invar alloy it

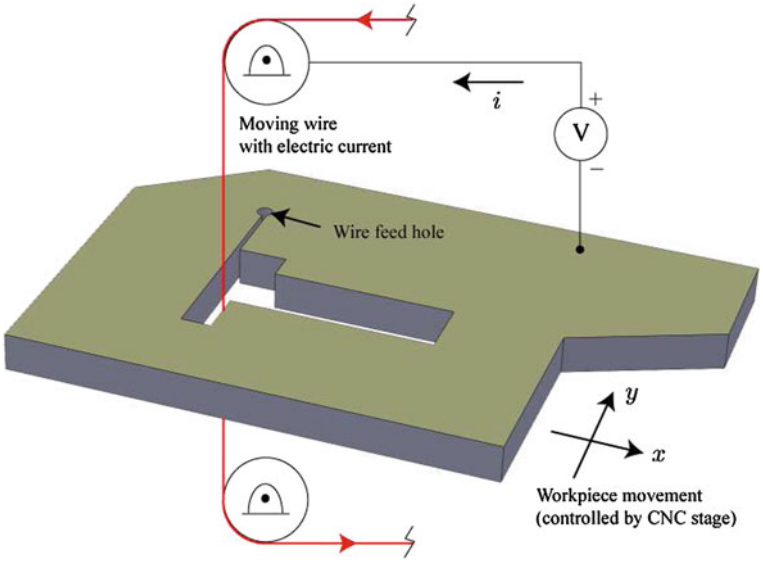

Fig. 4.12 Wire EDM machining process

is only 0.3×10^{-6} /°C, over 70 times lower. Best practices also include carefully matching the stage material with the materials of surround support structures. Also, materials with high thermal conductivity quickly reach thermal equilibrium, thus minimizing transient distortion during thermal expansion.

4.6 Manufacturing Techniques

The use of flexure mechanisms with stock piezoactuators require the ability to manufacture them. In general, the appropriate manufacturing technique for a given design and application depends on the scale of the positioning stage and the selected materials.

Standard milling, turning, and drilling techniques are best suited for metals, such as aluminum, titanium, and steel. These techniques are best for feature sizes above 1 mm, and they can achieve tolerances on the order of $\pm$ 0.001 in ($\approx$25.4 μm).

Monolithic flexures, especially those with complex shapes and intricate dimensions, are best created using wire electrical discharge machining (EDM). This method of machining was developed in the 1940s and is based on the erosion of a metallic material in the path of electrical discharges that form an arc between an electrode tool (wire) and the workpiece. As shown in Fig. 4.12, a basic EDM system consists of a wire electrode, a wire-feeding mechanism, and a conductive part that is moved relative to the wire in the lateral (x and y) directions using a numeric computer controlled

(CNC) stage. To create a cutout, a wire feed hole is first created where the wire is passed through the hole. During machining, debris is often flushed away from the cutting surface using an appropriate liquid. Wire diameters of approximately 100 μm are often used. Traditional machining techniques are often used to remove the bulk of the stock before performing EDM. Dimensional accuracy on the order of ±12 μm (± 0.0005 inch) can be achieved using the EDM process.

4.7 Design Example: A High-Speed Serial-Kinematic Nanopositioner

The design of a high-speed serial kinematic nanopositioner is described as an illustrative example. The nanopositioner is created for high-bandwidth applications that include video-rate scanning probe microscopy and high-throughput probe-based nanofabrication. The design offers approximately 9 × 9 × 1 μm range of motion and kHz bandwidth. Vertically stiff, double-hinged serial flexures are employed to guide the motion of the sample platform to minimize parasitic motion (runout) and off-axis effects (refer to Sect. 4.4.4). Additionally, the stage's out-of-plane stiffness is further improved by increasing the quantity of flexures n, decreasing the length L of each flexure, and thickening each flexure's center cross section. The effects of varying these parameters are examined in some detail. Along the vertical axis (z), a novel plate flexure guides the motion of the sample stage to minimize the effects of bending modes. Bending modes can significantly limit the positioning speed by causing the sample platform to rock side-to-side. It is pointed out for scanning-type applications, one lateral axis operates much faster than the other, and thus the serial-kinematic configuration is well-suited for these types of applications (Ando et al. 2008; Picco et al. 2007; Leang and Fleming 2009). Finally, the stage is integrated with a commercial scan-by-probe atomic force microscope and imaging and tracking results up to a line rate of 7 kHz are presented. At this line rate, 70 frames per second AFM video (100 × 100 pixels resolution) can be achieved.

4.7.1 State-of-the-Art Designs

A summary of existing multiaxis nanopositioning designs is listed in Table 4.2. One of the simplest and most effective way to achieve three-axis motion is to employ sectored tube-shaped piezoelectric actuators (Schitter and Stemmer 2004). However, the mechanical resonance of piezoelectric tube scanners is typically less than 1 kHz in the lateral scan directions, thus limiting the scan speed (Schitter and Stemmer 2004; Schitter et al. 2008; Fleming 2009; Rifai and Youcef-Toumi 2001). Additionally, the mechanical cross coupling causes undesirable SPM image distortion (Rifai and Youcef-Toumi 2001). In general, the maximum open-loop (without compensation)

Table 4.2 Summary of nanopositioner designs

Configuration	Range (μm)	Dominant Res. (kHz)	Imaging/line rate (range)
Tube scanner (Schitter and Stemmer 2004)	125 (x/y)	0.71 (x)	122 lines/s
		0.70 (y)	(13.5 × 13.5 μm)
Tube scanner	n/a	6.35 (x/y)	3 lines/s
Dual stage (z) (Schitter et al. 2008)		80 (z)	(25 μm)
Tube scanner	100 (x/y)	0.68 (x/y)	6.25 lines/s
Dual stage (z) (Fleming 2009)	10 (z)	23 (z)	(25 × 25 μm)
Shear piezo (Rost et al. 2005)	0.3 (x/y)	~64	80 frames/s
	0.20 (z)	>100	(128 × 128 px)
Flexure guided (Ando et al. 2008)	1 (x)	45	33 frames/s
	3 (y)		(100 × 100 px)
	2 (z)	360 ("self")	
Tuning fork (x)	<1 (x)	100	1000 frames/s
Flexure guided (y) (Picco et al. 2007)	2 (y)	40	(100 × 100 px)
Flexure guided (Schitter and Rost 2008)	13 (x/y)	>20	7810 lines/s
	4.3 (z)	33	(n/a)
Flexure guided (Yong and Aphale 2009)	25 (x/y)	2.73	n/a

positioning bandwidth is 1/100 to 1/10th of the dominant resonance (Clayton et al. 2009).

One of the earliest works on stiff mechanical nanopositioners was by Ando and co-workers (Ando et al. 2002), where stiff piezo-stack actuators were used to create a high-speed scanner. The researchers demonstrated imaging at 12.5 frames/s (100 × 100 pixels per image), and they used the system to capture real-time video of biological specimens (Ando et al. 2005). Shortly after, Schitter and co-workers also developed a scanner based on piezo-stack actuators, but in their design the actuators were arranged in a push-pull configuration and mechanical flexures were used to decouple the lateral and transverse motions (Schitter et al. 2007). They employed FEA to optimize the performance of the mechanical structure (Kindt et al. 2004). The reported AFM imaging rate is 8 frames/s (256 × 256 pixels). By exploiting the stiffness of shear piezos and a compact design, a scanner was created for imaging up to 80 frames/s (128 × 128 pixels) with a line rate of 10.2 kHz (Rost et al. 2005). The achievable range of motion is 300 × 300 nm. Another unique approach for high-speed scanning involves a piezo-stack actuator combined with a tuning fork as reported in Humphris et al. (2003). The tuning fork operated at resonance and AFM images were acquired at 100 frames/s (128 × 128 pixels). Likewise, a combined flexure-based scanner and tuning fork achieved imaging rate in excess of 1000 frames/s in Picco et al. (2007). Although the tip motion was fast, the range was limited and the trajectory was sinusoidal.

Flexure-guided piezoactuated scanning stages (Scire and Teague 1978), both direct drive serial-kinematic (Ando et al. 2008; Leang and Fleming 2009) and parallel-kinematic (Schitter et al. 2008) configurations, have been developed for

high-speed purposes. The advantages of flexure-guided scanners are high mechanical resonances and low cross-coupling. Multiple piezoactuators per degree-of-freedom have been used to increase range and bandwidth, but at the cost of increased power to drive the piezoactuators at high frequencies (Ando et al. 2008; Schitter et al. 2008). Designs which involve mechanical amplification have been implemented to increase range without having to increase the actuator's length (Scire and Teague 1978; Yong and Aphale 2009). However, the added mass of the mechanical amplifier along with the flexible linkages lowers the mechanical resonance. In general, a tradeoff must be made between range and bandwidth.

4.7.2 Tradeoffs and Limitations in Speed

The major tasks to design a high-speed nanopositioner include: (1) identifying relevant design parameters and tradeoffs, such as range of motion and maximum scanning bandwidth, (2) using FEA tools to optimize the mechanical structure, and (3) developing the necessary electronic hardware for the scanner. The design process is often iterative.

First, it is worth noting that range of motion conflicts directly with the achievable mechanical resonance. For example, large range requires large mechanical amplification A_f, which lowers the effective stiffness of the scanner (see Eq. (4.1)), and therefore the mechanical resonance (Kindt et al. 2004). One can expect that a piezo-driven nanopositioner with range of 1 μm or less will have a dominant mechanical in the hundreds of kHz range. For a positioner with a range between 1 and 5 μm, the mechanical resonance is often in the tens of kHz range. When the range is between 5 to 10 μm, the resonance falls to the kHz to tens of kHz range. Finally, ranges above 10 μm drop the mechanical resonance to the kHz and hundreds of Hz range. Most high-speed nanopostioners have operating range of less than 10 μm. This range of motion is still practical as it enables a scanner used in AFM to observe a wide spectrum of specimens and samples, from micron-size cells to submicron-size subjects such as DNA.

Video-rate SPM imaging requires a modest 30 frames per second, where each frame is at least 100 × 100 pixels. At this frame rate, the required linear scan rate is 3 kHz for the fast scan axis (along the x-direction, for example), and 30 Hz for the slow (y) axis. Faster scanning will increase frame rate, and/or frame resolution. The desired linear scan rate establishes a target for the dominant mechanical resonance in both axes. Assuming that the frequency of the command signals to drive the actuators must be at least 1/10th of the lowest resonance along each axis to avoid dynamic effects, the lowest mechanical resonance should be 300 and 30 kHz, for the y and x axis, respectively.

For comparison, the relationship between range and resonance frequency for a variety of commercial and custom nanopositioners is shown in Fig. 4.13 (Kenton 2010). The range is plotted with respect to the resonance frequency for each stage when provided. When full details are not provided for multiaxis positioners,

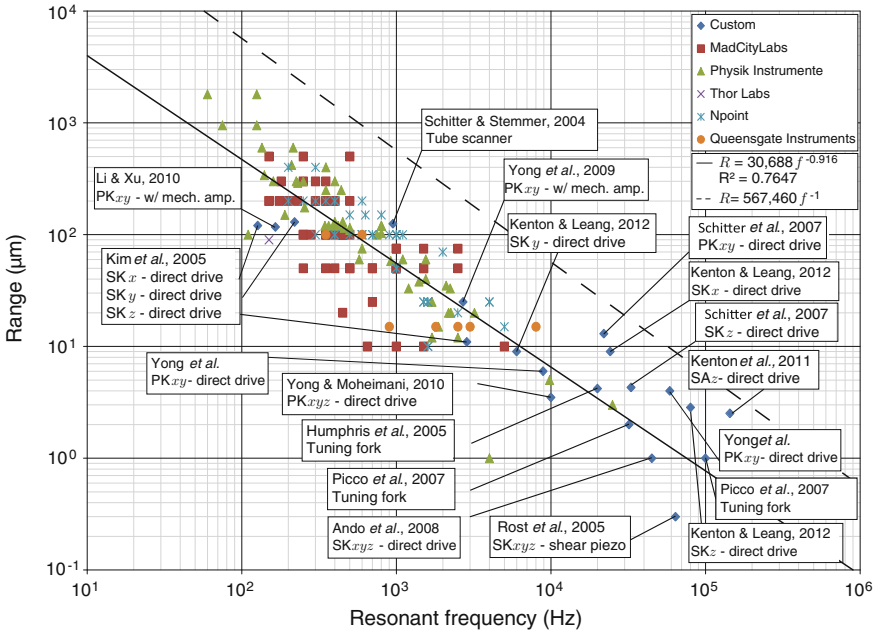

Fig. 4.13 High-performance commercial and custom nanopositioners plotted as range with respect to resonance frequency (adapted from Ref. Kenton (2010)). The *solid line* represents a linear least-square-error line fit to the data points. The *dashed line* represents the theoretical first mechanical resonance in the actuation mode for a fixed-free piezoactuator (assuming 1 μm of travel per 1 mm length). SK = serial-kinematic, PK = parallel-kinematic, SA = single-axis, x, y, z refers to axis being referenced

it is assumed that the resonance frequency is provided for the stage with the largest displacement, and therefore; the largest range is plotted with respect to the lowest resonance frequency. The dashed line in Fig. 4.13 marks the theoretical limit for a fixed-free piezoactuator with a modulus of elasticity of 33.9 GPa and a density of 8,000 kg/m^3 assuming 1 μm of travel per mm of piezo length (Kenton 2010). The commercial and custom nanopositioners in Fig. 4.13 are well below this theoretical limit. The solid line represents a fit to the data for commercial and custom nanopositioners.

The required power to drive the subject scanner must also be considered. The available power restricts the amount of voltage and current that can be delivered to the actuator. In turn, this restricts the type and dimensions of the piezoactuator that can be used for positioning. Larger piezoelectric actuators can provide greater stroke, but have higher capacitance and require more power at high frequencies.

Finally, cost and manufacturability must also be factored into the design. The scanner fabrication should not utilize any exotic materials or processes and should be tolerant of typical machining tolerances.

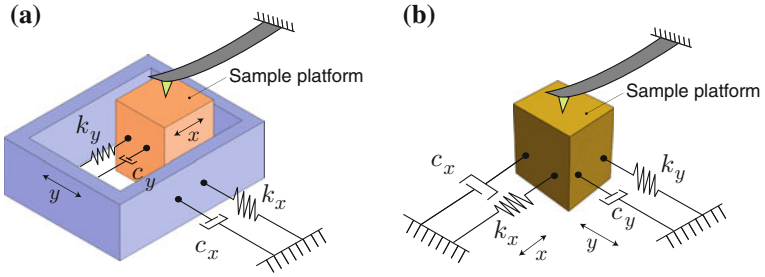

Fig. 4.14 Simplified models for two-axis scanning: **a** serial- and **b** parallel-kinematic configuration. The spring and damping constants include the effects of the piezoactuators and added flexures in each direction

4.7.3 Serial- Versus Parallel-Kinematic Configurations

For scanning in two directions, there are two basic configurations: serial and parallel kinematics as illustrated in Fig. 4.14. In a serial-kinematic system, for example the design used by several commercial vendors of scanning stages and in Ando et al. (2005), Kenton and Leang (2012), there is exactly one actuator (and sensor) for each degree of freedom (see Fig. 4.14a). One disadvantage of this design is the inability to measure (and correct for) parasitic motion such as runout or guiding error. Although the serial configuration is simple to design, a penalty is that high resonance frequency can only be achieved in one axis.

In a parallel-kinematic scanning stage, e.g., Schitter et al.'s work (Schitter 2007), all actuators are connected in parallel to the sample platform (see Fig. 4.14b). This arrangement enables rotation of the image, i.e., the fast scanning axis can be chosen arbitrarily. An advantage of this configuration is that parasitic motion due to runout and guiding error can easily be measured and corrected. However, since the mechanical dynamics of both the lateral and transverse axes are similar, high-bandwidth control hardware is required for both directions. In contrast, for the serial-kinematic configuration only the high-speed axis requires high power and wide bandwidth performance, reducing overall cost.

In the simplified model shown in Fig. 4.14, the effective stiffnesses and damping effect for both the serial and parallel kinematic configurations include the flexures and the actuators along each direction. To achieve high resonance frequencies, the effective stiffnesses should be a high as possible while achieving the desired range of motion. The effects of inertial force generated by the sample platform during scanning must also be taken into account. The flexures must provide enough preload to avoid exposing the stack actuator to damaging tensional forces.

While the resonance frequency of the fast axis is of primary concern, the slow-axis resonance frequency can essentially be ignored. For example, the scan rate of the slow axis is one-hundredth the scan rate of the fast-axis when acquiring a 100×100 pixel image. Therefore, the fast scan axis can be designed independently without any

Table 4.3 Comparison of plate-stack piezoactuators

Size (mm)	Free stroke (μm)	Cap. (nF)	k_a (N/μm)	k_z* (N/μm)	k_z/k_a
3 × 3 × 10	11.15	114	30.5	2.0	0.066
5 × 5 × 10	11.78	387	84.8	10.7	0.126
7 × 7 × 10	12.09	835	166.1	28.0	0.169
10 × 10 × 10	12.13	1673	339.0	69.2	0.204

* Stiffness for fixed-guided beam accounting for shear (see Sect. 4.7.6)

significant consideration for performance implications on the slow-scan axis. As previously stated, for scanning-type applications, one lateral axis operates much faster than the other, and thus the serial-kinematic configuration is well-suited for these types of applications (Ando et al. 2008; Picco et al. 2007; Leang and Fleming 2009).

4.7.4 Piezoactuator Considerations

The actuating mechanism of choice for scanning at high speed is the piezoactuator (Kenton and Leang 2012), particular piezo-stack actuators. Although thin shear-piezos offer higher mechanical resonances, their range is rather limited (sub-micron level) (Rost et al. 2005). Piezo-stack actuators are stiff and compact. A comparison of four plate-stack piezoactuators (Noliac) of varying cross-sectional areas is shown in Table 4.3. Each actuator in this comparison is 10-mm long and meets the desired free stroke of 11 μm. (A small percentage of the free stroke will be lost due to flexure stiffness and boundary conditions associated with gluing the piezo-stack to the stage during assembly.) The capacitance increase is nearly proportional to the cross-sectional area with an average of 15.5 nF/mm^2 (for a 10-mm long piezo-stack actuator). The Young's modulus is calculated from the blocking force and free stroke. For instance, the Young's modulus of a 5 × 5 × 10 mm piezoactuator is determined to be 33.9 GPa (Leang and Fleming 2009). As shown in Table 4.3, higher actuation and out-of-plane stiffness can be obtained by using larger (cross-section) piezo-stacks. The cost, however, is higher capacitance which increases the net power to drive the actuators, especially at high frequencies.

To achieve the desired scan range of 10 × 10 μm, a piezoelectric stack actuator with dimensions of 5 × 5 × 10 mm and capacitance of 387 nF is chosen (e.g., Noliac SCMA-P7). Figure 4.15 shows a photograph of the piezo-stack actuator to drive the high- and low-speed stages. The actuator stroke is 11.8 μm, with an unloaded resonance frequency of 220 kHz, stiffness of 283 N/μm, blocking force of 1000 N, and maximum drive voltage of 200 V. The elastic modulus calculated from the blocking pressure P_B and strain ϵ is $E = \frac{P_B}{\epsilon} = 33$ GPa.

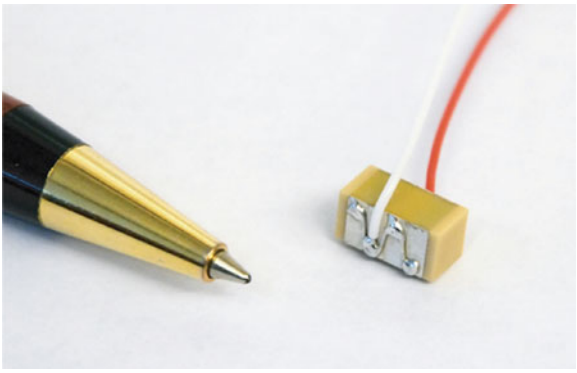

Fig. 4.15 A photograph of the piezo-stack actuator used to drive the x and y stage

4.7.5 Preloading Piezo-Stack Actuators

As discussed in Sect. 2.5.3, piezo-stacks are intolerant to tensile (as well as shear) stresses. Because stacks are constructed of glued (or fused) piezoelectric layers, tensional loads can cause the actuators to fail at the interface (glue) layers. Manufacturers often specify a tensile load limit less than 10 % of the compressive load limit. During high-speed operation, inertial forces due to the sample mass must be taken into account to avoid excessive tensile stresses. A preload force must be incorporated to eliminate the possibility of the actuator being exposed to excessive tensile forces. The preload must be applied in such a way that full surface contact is achieved to assure good load distribution (see Fig. 2.9). Recommended preload force is 20 % of the compressive load limit of the actuator, and the preload spring stiffness should be at most 10 % of the actuator stiffness.

Flexures can be used to apply the appropriate preload on the piezo-stack actuator to compensate for the inertial force during dynamic operation. The flexures serve two purposes: to eliminate tensile stress and to guide the extension/contraction of the actuator so that parasitic motion is minimized. The required preload is estimated from Newton's Second Law by computing the maximum sample platform acceleration during maximum excursion and scan frequency. In particular, the magnitude of the expected dynamic (inertial) force on a piezoactuator assuming sinusoidal motion at frequency f (in Hz) is given by

$$F_i = 4\pi^2 m_{\text{eff}} \left(\frac{\Delta x}{2} \right) f^2, \tag{4.37}$$

where m_{eff} is the effective mass and Δx is the total stroke length. For example, a 5 g sample positioned over a 10 μm range at 3,000 Hz, the minimum preload requirement is 8.9 N. Considering a safety factor of 2, the required preload is at least 18 N.

4.7.6 Flexure Design for Lateral Positioning

The basic layout for a serial-kinematic design is shown in Fig. 4.16, where the high-speed (x-axis) stage is nested inside of the low-speed (y-axis) stage (Fig. 4.16a, b). The stage body is manufactured from 7075 aluminum using the wire EDM process to create a monolithic platform. The sample platform is located on the x-stage body, and vertical motion is achieved with a piezo-stack actuator embedded into the x-stage body (Ando et al. 2008) (see details in Fig. 4.16c). Compliant flexures with improved vertical-stiffness to minimize out-of-plane motion are used to guide the motion of the sample platform. The flexures are strategically placed to minimize the sample platform's tendency to rotate (θ_x, θ_y, θ_z) at high frequencies. Also, the stage is designed to ensure that the first resonance in all three axes are axial (piston) modes, rather than off-axis modes, which can severely limit performance.

For translational motion, u_i ($i = x,\ y,\ z$), the single degree-of-freedom mechanical resonance is given by $f_{u_i,0} = \frac{1}{2\pi}\sqrt{\frac{k_i}{m_i}}$, where m_i and k_i are the effective translational mass and stiffness, respectively. Likewise for rotational motion, θ_i ($i = x,\ y,\ z$), the first resonance is $f_{\theta_i,0} = \frac{1}{2\pi}\sqrt{\frac{k_{\theta_i}}{J_i}}$, where J_i and k_{θ_i} are the effective mass moment of inertia and rotational stiffness, respectively. To insure that actuation modes occur before the out-of-plane modes, the strategy taken is to optimize the stage geometry and flexure configuration so that the out-of-plane stiffness-to-mass ratios ($k_z/m_z, k_{\theta y}/J_y, k_{\theta z}/J_z$) are higher than the actuation stiffness-to-mass ratio k_x/m_x. Figure 4.17 shows the simplification of a high-speed x-stage into single degree-of-freedom systems to model four of the dominating resonance modes. The top and side views are broken down to show the effective springs and masses affecting the body for (d) actuation u_x, (e) and (f) rotation θ_z and θ_y, and (g) vertical u_z modes. Damping is omitted for convenience.

The vertical stiffness of the x- and y-stages is increased by (1) increasing the number of flexures, (2) utilizing shorter (effective length) flexures, and (3) converting the flexures from constant rectangular cross section beam flexures to a serial-compliant double-hinged flexure with a "rigid" center connecting link (see Fig. 4.9). The first step taken to increase the flexure stiffness in the vertical direction is studying how the total number of flexures n used in parallel, flexure thickness t, and length L affect the vertical stiffness k_z for a given actuation stiffness k_a. This comparison is done analytically and using finite element analysis (COSMOSWorks FEA).

The stiffness of a flexure is defined as the ratio of a load F and the resulting displacement u. The displacements and loads are: translational displacement u_i, rotational displacement θ_i, translational force F_i acting on a point in the i direction, and moment M_i (torque T) acting about the i axis (θ_i), respectively, where $i = x, y, z$. Figure 4.7 illustrates the corresponding directions of the displacements and loads acting on the free end of a fixed/free cantilever beam which models a beam flexure. The in- and out-of-plane compliances for a fixed/free beam is derived using Castigliano's second theorem (Timoshenko 1953; Lobontiu 2003; Craig 2000). The compliance equations are then used to derive equations for the actuation and vertical

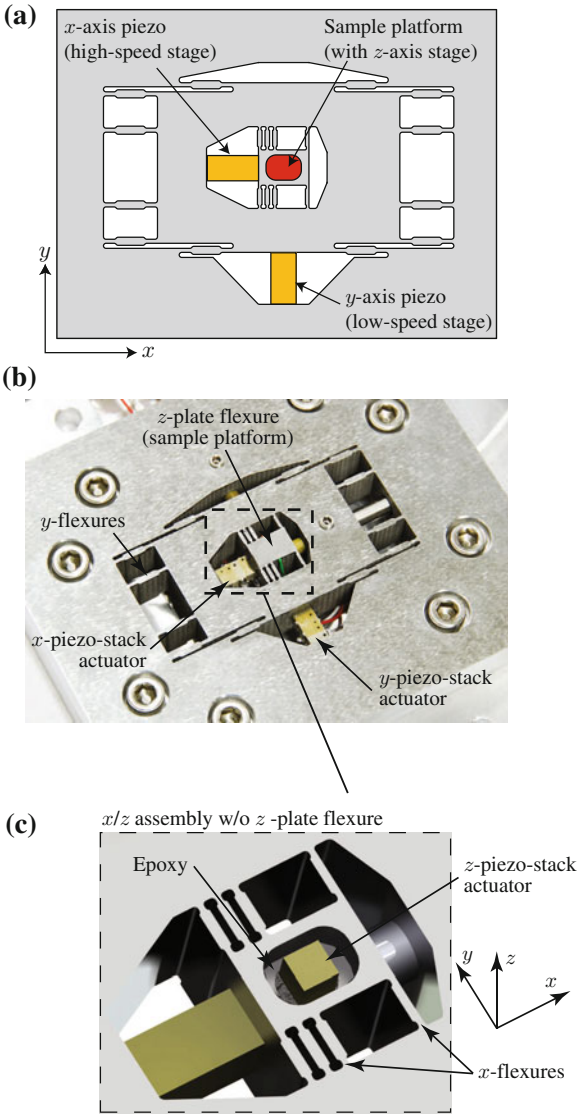

Fig. 4.16 A serial-kinematic nanopositioner: **a** *top view*, **b** fabricated stage, and **c** details of the sample platform and z-stage

stiffness k_i of a fixed/roller guided beam shown in Fig. 4.18a1 through a3. It is pointed out that the fillet radius is considerably smaller compared to the flexure length and therefore has minimal effect on the flexure stiffness. For this reason, to simplify the flexure stiffness equations in this initial analysis, the compliance equations are derived for a beam with a constant cross sectional thickness.

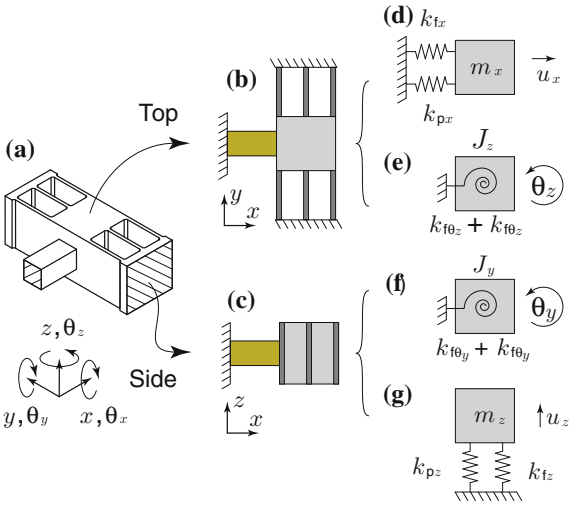

Fig. 4.17 Generic flexure-guided stage simplified to single degree-of-freedom systems modeling the dominant modes

For a fixed/free beam of rectangular cross section, the total strain energy is

$$\begin{aligned} U &= U_{\text{axial}} + U_{\text{torsion}} + U_{\text{bending}} + U_{\text{shear}} \\ &= \int_0^L \left[\frac{F^2}{2AE} + \frac{T^2}{2GJ} + \frac{M^2}{2EI} + \frac{\alpha V^2}{2GA} \right] \mathrm{d}x, \end{aligned} \tag{4.38}$$

where L is the beam length, A is the cross sectional area of the beam, h is the height, t is the thickness, E is Young's modulus, $G = \frac{E}{2(1+\nu)}$ is the shear modulus, ν is Poisson's ratio, $J = ht^3 \left[\frac{1}{3} - 0.21 \frac{t}{h} \left(1 - \frac{t^4}{12h^4} \right) \right]$ is the approximate torsional moment of inertia (Young and Budynas 2002), $I = \frac{ht^3}{12}$ is the second moment of inertia about the vertical z axis, V is the shear force, and α is a shape factor for the cross section used in the shear equation (for a rectangular cross section $\alpha = 6/5$) (Craig 2000; Young and Budynas 2002; Park 2005).

Applying Castigliano's second theorem, the displacement of a point in a given direction u_i, θ_i is the partial derivative of the total strain energy with respect to the applied force, i.e.,

$$u_i = \frac{\partial U}{\partial F_i}; \qquad \theta_i = \frac{\partial U}{\partial M_i}. \tag{4.39}$$

From here the compliance is simply found by dividing the displacement by the applied load, i.e.,

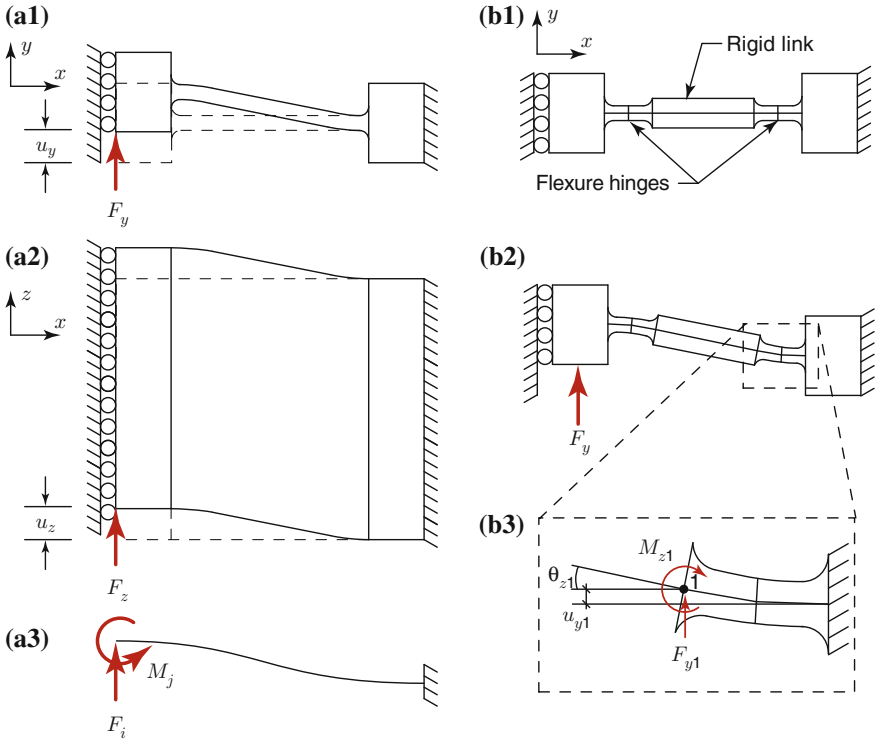

Fig. 4.18 Corner-filleted and center-thickened flexures showing loads and deformations: **a1** *top* and **a3** *side views* showing displacement caused by force F_i, for $i = x,\ y$, in a fixed/guided end configuration, and **a3** loads acting on the free end of a fixed/free beam for a corner-filleted. **b1** *top view*, **b2** *top view* with applied load, and **b3** expanded view of corner-filleted flexure hinge

$$C_{u_i,F_j} = \frac{u_i}{F_j}; \qquad C_{\theta_i,M_j} = \frac{\theta_i}{M_j}. \tag{4.40}$$

For example, the compliance of the rectangular cross section fixed-free beam in Fig. 4.7a due to a point load in the y direction starts with the total strain energy

$$U = \int_0^L \frac{M(x)^2}{2EI(x)}\,\mathrm{d}x + \int_0^L \frac{\alpha V(x)^2}{2GA(x)}\,\mathrm{d}x, \tag{4.41}$$

where $A(x)$ and $I(x)$ are constant. The coordinate system is placed on the free end of the flexure as shown in (Lobontiu 2003) where the shear is $V(x) = F_y$ and moment is $M(x) = F_y x$. The total strain energy for the applied load is

$$U = \frac{F_y^2}{2EI}\int_0^L x^2\,\mathrm{d}x + \frac{\alpha F_y^2}{2GA}\int_0^L \mathrm{d}x = \frac{F_y^2 L^3}{6EI} + \frac{\alpha F_y^2 L}{2GA}. \tag{4.42}$$

Therefore, the resultant displacement is

$$u_y = \frac{\partial U}{\partial F_y} = \frac{F_y L^3}{3EI} + \frac{\alpha L F_y}{GA}, \tag{4.43}$$

and the compliance is

$$C_{22} = \frac{u_y}{F_y} = \frac{L^3}{3EI} + \frac{\alpha L}{GA}. \tag{4.44}$$

The compliances are then used to form the compliance matrix $\mathbf{C}$ which is defined as the ratio of the displacement $\mathbf{U} = \begin{bmatrix} x & y & \theta_z & z & \theta_y & \theta_x \end{bmatrix}^T$ for a given load $\mathbf{L} = \begin{bmatrix} F_x & F_y & M_z & F_z & M_y & M_x \end{bmatrix}^T$, hence the displacement vector is

$$\begin{Bmatrix} u_x \\ u_y \\ \theta_z \\ u_z \\ \theta_y \\ \theta_x \end{Bmatrix} = \begin{bmatrix} C_{11} & 0 & 0 & 0 & 0 & 0 \\ 0 & C_{22} & C_{23} & 0 & 0 & 0 \\ 0 & C_{23} & C_{33} & 0 & 0 & 0 \\ 0 & 0 & 0 & C_{44} & C_{45} & 0 \\ 0 & 0 & 0 & C_{45} & C_{55} & 0 \\ 0 & 0 & 0 & 0 & 0 & C_{66} \end{bmatrix} \begin{Bmatrix} F_x \\ F_y \\ M_z \\ F_z \\ M_y \\ M_x \end{Bmatrix}. \tag{4.45}$$

For a constant cross section fixed/free beam the compliances are $C_{11} = \frac{L}{AE}$, $C_{22} = \frac{L^3}{3EI} + \frac{\alpha L}{GA}$, $C_{23} = \frac{L^2}{2EI}$, $C_{33} = \frac{L}{EI}$, $C_{44} = \frac{4L^3}{Eh^3t} + \frac{\alpha L}{GA}$, $C_{45} = \frac{6L^2}{Eh^3t}$, $C_{55} = \frac{12L}{Eh^3t}$, and $C_{66} = \frac{L}{GJ}$. For a long slender beam, shear strain has little effect and therefore can be ignored in C_{22}. For a short beam with a significant height-to-length aspect ratio, such as the vertical displacement of the flexure shown in Fig. 4.18a2, much of the deflection is in shear, and therefore can not be ignored.

The displacement vector equation presented above is used to solve for the actuation stiffness k_y and vertical stiffness k_z of a fixed/guided flexure beam, i.e., $F_i/u_i = k_i$. Torsional stiffness is not investigated because the θ_x rotational mode is largely dependant upon the vertical flexure stiffness when the flexures are placed at the corners of the stage body. Figure 4.18a3 shows the applied load and the expected deflection curve of the flexure in both the (a1) actuation direction and (a2) vertical direction. The active load being applied to the flexure is the in-plane force F_i. The resultant moment $M_j = -F_i L/2$ is caused by the roller-guided end constraint. Therefore, the flexure displacement in the actuation direction u_y due to the applied force F_y and moment $M_z = -F_y L/2$ is

$$u_y = C_{22}F_y + C_{23}M_z = C_{22}F_y - C_{23}F_yL/2$$
$$= F_y\left[\frac{L^3}{3EI} + \frac{\alpha L}{Ght} - \frac{L}{2}\frac{L^2}{2EI}\right]. \tag{4.46}$$

Taking the ratio of the applied load to the displacement, the actuation stiffness (neglecting shear) is

$$k_y = \frac{F_y}{y} = \left[\frac{L^3}{12EI} + \frac{\alpha L}{Ght}\right]^{-1} \cong \frac{12EI}{L^3}. \tag{4.47}$$

Using the same method, the displacement of the flexure in the vertical direction u_z is

$$u_z = C_{44}F_z + C_{45}M_y = C_{44}F_z - C_{45}F_zL/2$$
$$= F_z\left[\frac{4L^3}{Eh^3t} + \frac{\alpha L}{Ght} - \frac{L}{2}\frac{6L^2}{Eh^3t}\right]. \tag{4.48}$$

Similarly, the vertical stiffness is

$$k_z = \left[\frac{L^3}{Eh^3t} + \frac{\alpha L}{Ght}\right]^{-1}. \tag{4.49}$$

Because of the high aspect ratio in the vertical direction, shear cannot be ignored.

Equations (4.47) and (4.49) are used to study the effect of the quantity of flexures n and flexure thickness t on the effective vertical out-of-plane stiffness $k_{z\,\text{eff}}$. To do this, the desired actuation stiffness $k_{y\,\text{eff}} = 10$ N/μm is divided amongst the number of flexures n to give the actuation stiffness for an individual flexure $k_{y\,i}$. From there, Eq. (4.47) is used to determine the length L for $t \in [0.3, 1]$ mm. The individual vertical stiffness $k_{z\,i}$ is then calculated using Eq. (4.49). The effective vertical stiffness is $k_{z\,\text{eff}} = \sum^n k_{z\,i}$. By increasing the number of flexures from 2 to 12 (1-mm thick) the vertical stiffness is increased from 76 to 226 N/μm (197 % increase). For $n = 2$, decreasing the flexure thickness from 1 to 0.3-mm thick (which effectively decreases the flexure length) increased the vertical stiffness from 76 to 79.5 N/μm (4.6 % increase). Increasing the number of flexures from 2 to 12 and decreasing the flexure thickness from 1 to 0.3-mm thick produces a vertical stiffness of 260 N/μm (242 % increase). In Fig. 4.19, the circles denote the $k_{z\,\text{eff}}$ values obtained using FEA. The FEA results follow the trend of the analytical results with the only variance being an increase in effective stiffness (average increase = 3.15 %). Increasing flexure height h also contributes to increasing vertical stiffness but at the cost of a taller stage body, which increases the mass m thus reducing the actuation resonance.

The most dramatic increase in vertical stiffness for a beam flexure is observed by increasing the number of flexures n. Decreasing the flexure thickness (and as a result, the flexure length) increases the vertical stiffness as well. But the limiting factor of

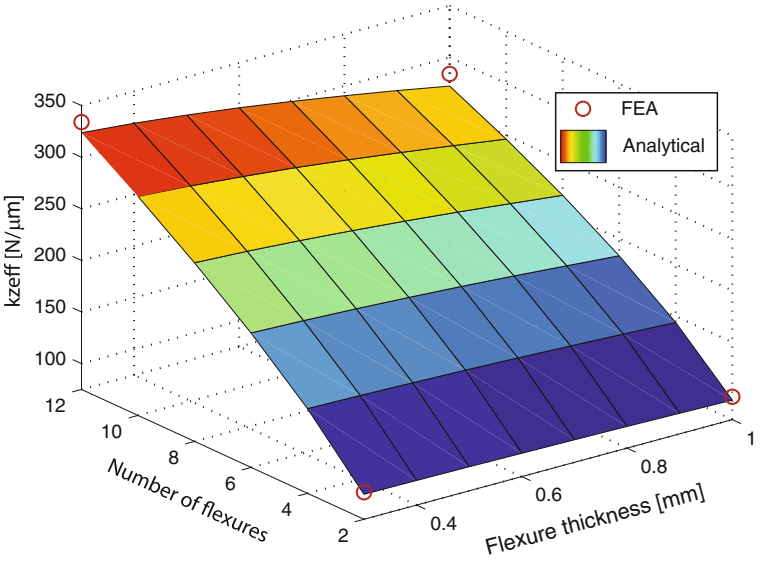

Fig. 4.19 FEA and analytical results showing effective vertical flexure stiffness $k_{z\ \mathrm{eff}}$ with respect to flexure thickness t and quantity of flexures n. Effective actuation stiffness $k_{y\ \mathrm{eff}}$ is held constant at 10 N/μm

decreasing the flexure thickness is stress. A shorter thinner beam flexure will have higher stress concentration than a longer thicker beam flexure of equal stiffness.

When a corner-filleted beam flexure, as studied above, is displaced in the actuation direction, the majority of the strain is located at the flexure ends near the fillets. Additionally, when the same flexure is displaced in the vertical direction, the majority of the vertical displacement is in shear strain located at the center cross-section. An effective way to further increase the out-of-plane stiffness of a beam flexure is to increase the thickness of the center section of the flexure, thus converting the beam flexure into a double-hinged serial flexure as shown in Fig. 4.9. Both analytical and FEA methods are used to study the vertical stiffness of the 'thickened' flexures. The cross-sectional area and second moment of inertia values in Eq. (4.41) are replaced with $A(x) = ht(x)$ and $I(x) = ht(x)^3/12$, respectively. For example, the thickness of the flexure in Fig. 4.9 is

$$t(x) = \begin{cases} t + 2\left[r - \sqrt{x(2r-x)}\right], & x \in [0, a] \\ t, & x \in [a, b] \\ t + 2\left[r - \sqrt{(l-x)(2r-l+x)}\right], & x \in [b, c] \\ t + 2r, & x \in [c, d] \\ t + 2\left[r - \sqrt{(l-g)(2r-l+g)}\right], & x \in [d, e] \\ t, & x \in [e, f] \\ t + 2\left[r - \sqrt{g(2r-g)}\right], & x \in [f, L] \end{cases} \tag{4.50}$$

Table 4.4 y-axis flexure stiffness comparison

Type	$k_{y\ \mathrm{eff}}$ (N/μm)		$k_{z\ \mathrm{eff}}$ (N/μm)	
	Analytical	FEA	Analytical	FEA
Filleted beam	5.82	6.00	196.6	213.9
Thickened center	5.84	5.32	237.6	238.2

where $a = r$, $b = l - r$, $c = l$, $d = L - l$, $e = d + r$, $f = L - r$, $g = L - x$, t and l are thickness and length of the thin section of the flexure, r is the fillet radius, $t + 2r = T$ is the thickness of the thickened section, and L is the length of the entire flexure. For this case, the compliance is determined by first determining the total strain energy (Eq. 4.41) while using the thickness function $t(x)$ in the area $A(x)$ and second moment of inertia $I(x)$ expressions. Again, the coordinate system is placed on the free end for simplification and to allow for direct integration as shown in (Lobontiu 2003). For instance, the total strain energy for bending due to a point load is

$$\begin{aligned} U &= \int_0^L \frac{M(x)^2}{2E\frac{ht(x)^3}{12}}\,\mathrm{d}x + \int_0^L \frac{\alpha V(x)^2}{2Ght(x)}\,\mathrm{d}x, \\ &= \frac{12F_y^2}{2Eh}\int_0^L \frac{x^2}{t(x)^3}\,\mathrm{d}x + \frac{\alpha F_y^2}{2Gh}\int_0^L \frac{1}{t(x)}\,\mathrm{d}x. \end{aligned} \tag{4.51}$$

Taking the partial derivative with respect to the applied force F_y gives the displacement

$$u_y = \frac{\partial U}{\partial F_y} = \frac{12F_y}{Eh}\int_0^L \frac{x^2}{t(x)^3}\,\mathrm{d}x + \frac{\alpha F_y}{Gh}\int_0^L \frac{1}{t(x)}\,\mathrm{d}x. \tag{4.52}$$

The in-plane (and out-of-plane) stiffness is then calculated numerically by taking the ratio of the force to deflection. Table 4.4 compares the actuation and vertical stiffness of a standard filleted flexure beam to a thickened flexure beam obtained analytically and using FEA. This comparison shows how the vertical stiffness of beam flexures similar to the ones used on the y-stage can be increased an additional 19.3 % by simply increasing the thickness of the center section. To keep the actuation stiffness $k_{y\ \mathrm{eff}}$ constant, the length L of the thickened flexure is increased from 9.75 mm to 10.70 mm.

In summary, the effective vertical stiffness can be improved to increase the out-of-plane stiffness by (1) increasing the number of flexures n, (2) decreasing the flexure length L, and (3) thickening the center section of a beam flexure to create a serial-compliant double-hinged flexure.

Flexure placement is important to help increase rotational stiffness. Increasing the length (and width) of a stage and placing flexures at the corners of the moving

platform increase rotational stiffness of the platform. However, the cost of increasing the size of the platform is increasing overall mass, thus lowering the mechanical resonance.

The first five modes for the x- y- and z-stages are predicted using the *frequency* tool in COSMOSWorks (FEA). (Detailed discussion of the z-stage design is presented below.) It is assumed that the resonances of the y-stage would not be excited by the dynamic motion of the inner nested x-stage. This allows the design shown in Fig. 4.20a to be broken down into the low-speed y-stage (Fig. 4.20b1–b5), high-speed x-stage (Fig. 4.20c1–c5), and vertical z-stage (Fig. 4.20d1–d5). The boundary faces of each stage (shown hatched) have a fixed boundary condition. All contacting components are bonded together with compatible mesh. The meshing is done at "high quality" with refined meshing at the flexure fillets and pivot points (0.25 mm minimum element size on surfaces). The materials used and their corresponding mechanical properties are as follows:

- Aluminum: $E = 72$ GPa, $\nu = 0.33$, $\rho = 2700$ Kg/m^3;
- Steel: $E = 200$ GPa, $\nu = 0.28$, $\rho = 7800$ Kg/m^3;
- Piezo-stack: $E = 33.9$ GPa, $\nu = 0.30$, $\rho = 8000$ Kg/m^3;
- Alumina: $E = 300$ GPa, $\nu = 0.21$, $\rho = 3960$ Kg/m^3,

where the modulus for the piezo-stack was calculated from the stiffness and blocking force. The predicted first mechanical resonance for the y-, x-, and z-stage are 5.96, 25.9, and 113 kHz, respectively, all of which are in the corresponding stage actuation direction as preferred. Simulated FEA frequency response is done using the *Linear Dynamic (Harmonic)* tool in COSMOSWorks. A constant amplitude sinusoidal force is applied in the actuation direction at the corners of the piezoactuator/stage interfaces. The force generated is assumed proportional to the applied voltage. A global modal damping ratio of 0.025 is applied to simulate the damping of aluminum alloy and to produce a gain of 20 dB. Figure 4.21a1, b1 show the predicted frequency response plots for the x- and y-axis with the resonant peaks occurring at 25.9 and 5.96 kHz, respectively.

4.7.7 Design of Vertical Stage

The quick movements of the z-stage when tracking sample features such as steps, may excite the resonance modes of the nesting x-stage. To minimize impulsive forces along the vertical direction, a dual counterbalance configuration is utilized. Ando et al. (2008) describe four configurations which include face mounting, mounting both faces of the actuator to flexures, and inserting the piezoactuator in a hole and allowing the end faces to be free. Dual face-mounted z-piezoactuators are a simple and effective method for counterbalancing. However, the disadvantage is the first resonance mode for a slender piezoactuator is bending as shown in Fig. 4.22a1, instead of the desired actuation mode as illustrated in Fig. 4.22a2. Inserting the piezoactuator into a hole in

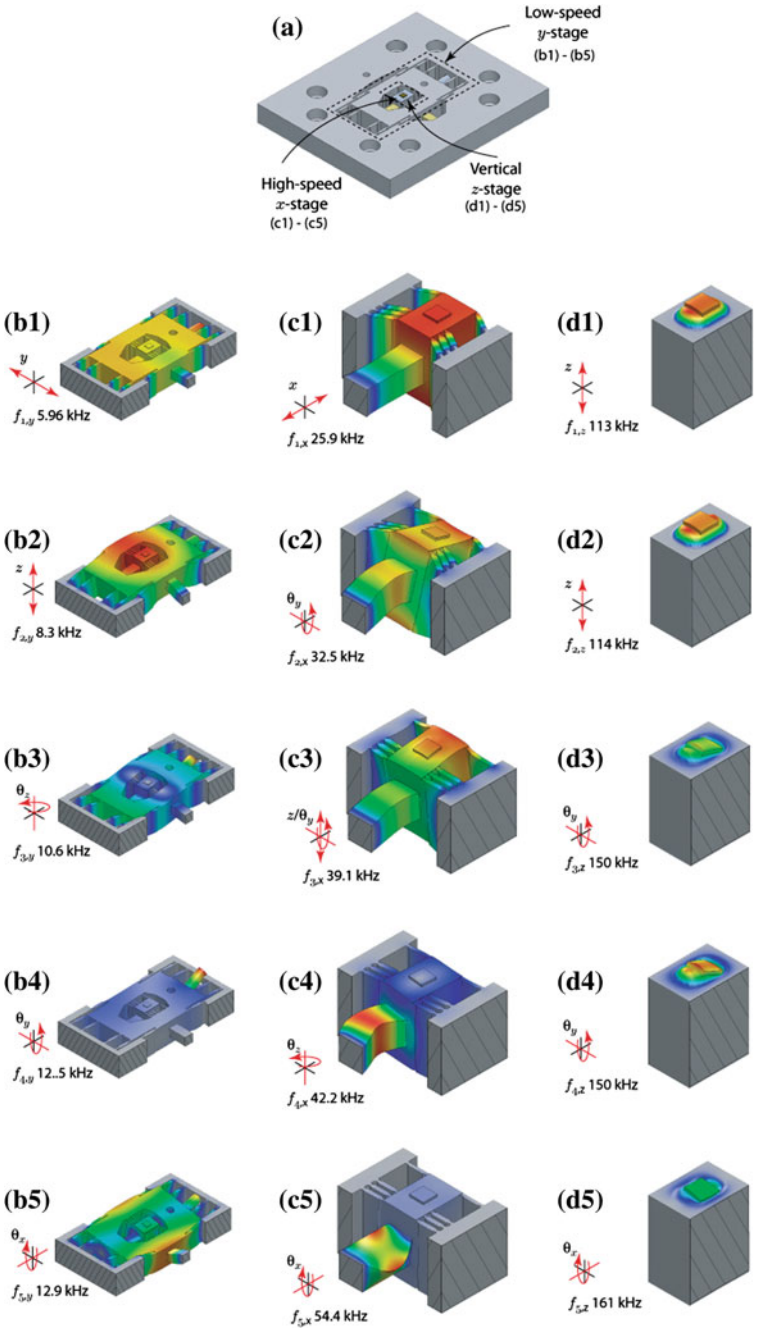

Fig. 4.20 Finite element analysis results showing first five modes: **a** high-speed scanning stage; **b1**–**b5** low-speed *y*-stage; **c1**–**c5** high-speed *x*-stage; and **d1**–**d5** *vertical z*-stage. Each stage section is designed to have the first mechanical resonance to occur in the actuation direction

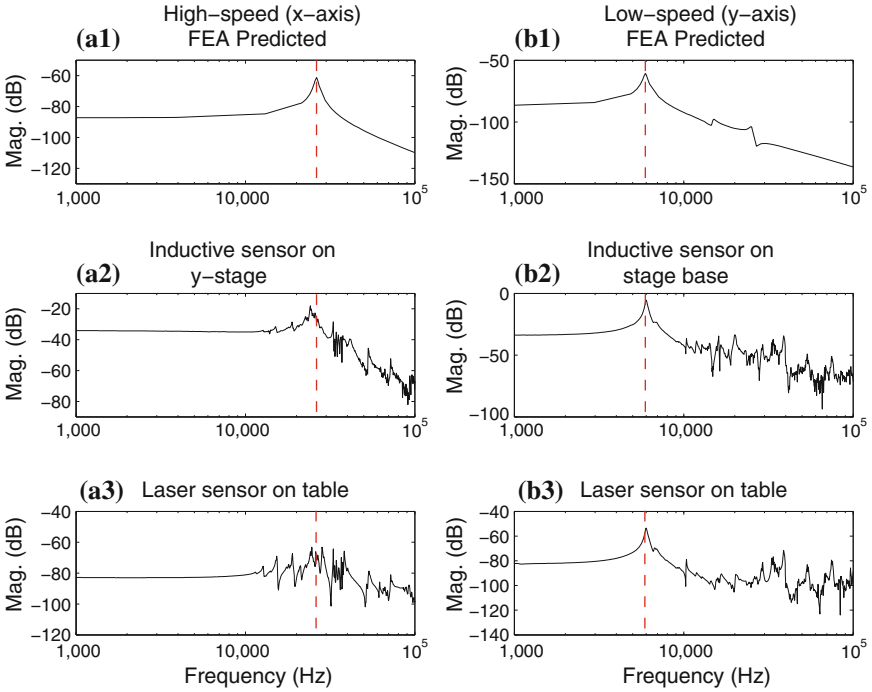

Fig. 4.21 **a1**–**a3** Comparison of predicted and measured frequency response functions for the high-speed stage (x-axis), **b1**–**b3** the low-speed stage (y-axis). The *vertical dashed line* is used to compare the experimentally measured results to the FEA predicted first resonance peak

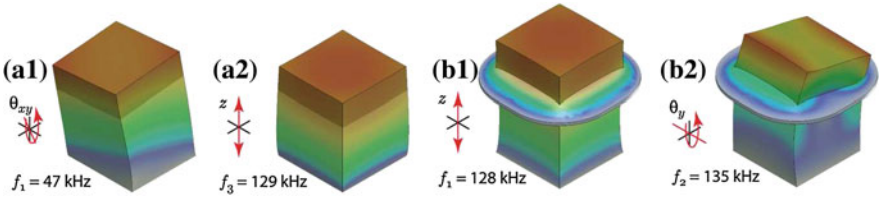

Fig. 4.22 FEA results for z-piezo with 1-mm thick sample, **a** without and **b** with flexure

the x-stage is tested, but unfortunately the design requires a long piezoactuator and did not constrain the end faces well.

A new configuration as shown in Fig. 4.23 is proposed in which a dual face-mounted piezo arrangement is combined with a compliant end plate flexure. The piezoactuators are first recessed within the nesting stage so that the free face is flush with the top surface of the stage body. The plate flexure is glued to the free end of the piezoactuator and the surrounding surface of the stage. Figure 4.22b1, b2) show how by using a plate flexure, the bending (and torsional) modes can be shifted above the frequency of the actuation mode.

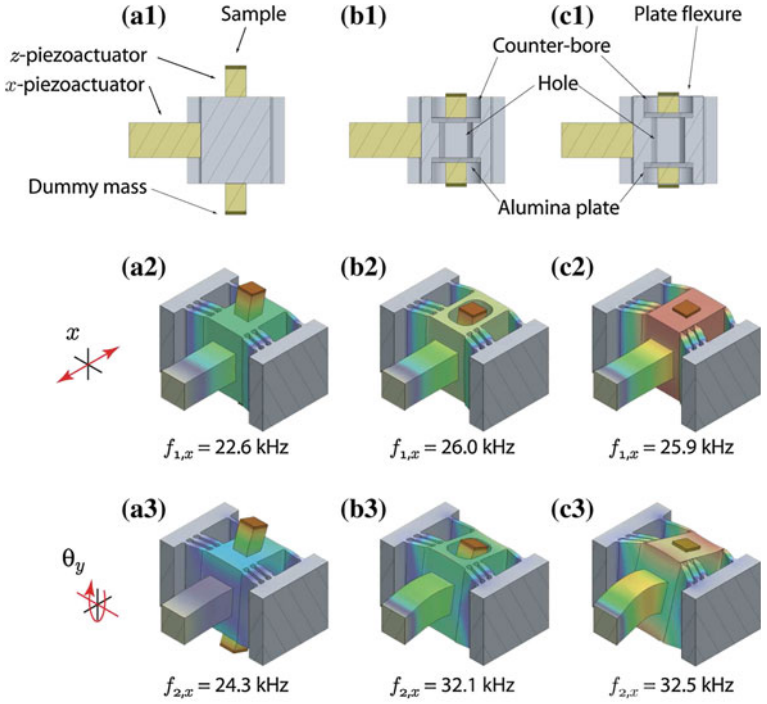

Fig. 4.23 Three configurations for the z-piezoactuator and corresponding first two modes. The dynamic characteristics of the face-mounted configuration in **a** are improved by **b** recessing the z-piezoactuator into the x-stage body and **c** adding a plate flexure to the free face of the z-actuator **c**

4.7.8 Fabrication and Assembly

The main stage body of the scanner is constructed from a single block of 7075 aluminum alloy, where the features are machined using traditional milling and wire EDM processes. The x- and y-stages are displaced with $5 \times 5 \times 10$ mm Noliac SCMAP07 piezo-stack actuators, where the motion is guided by compliant, center-thickened flexures described above. The x-flexures are designed to have a pivot point thickness of 0.5 ± 0.03 mm to produce an effective axial stiffness of 14 ± 2 N/μm. When assembling the x- and y-stages, it is important to preload the piezoactuators. Failure to preload will result in lower mechanical resonances that resemble the predicted free stage resonance (stage without piezoactuator). Preloading is accomplished by initially displacing the stages in the actuation direction and sliding the piezoactuators in place, then applying shims and glue. The tension on the stage is then released onto the piezoactuator resulting in preload. Other preload mechanisms include set-screws and spring-based mechanisms.

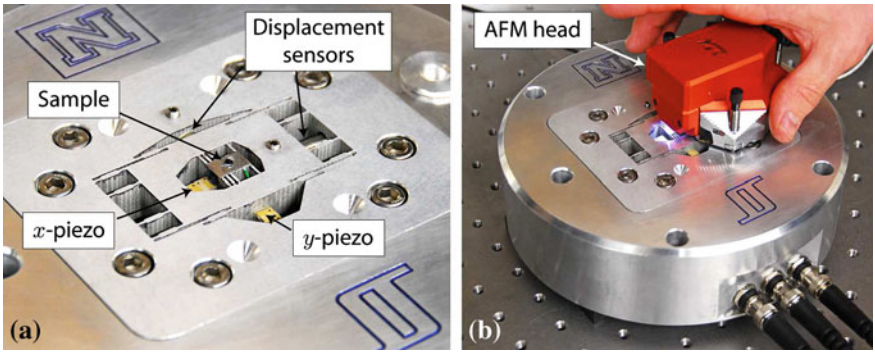

Fig. 4.24 Assembled positioner: **a** stage with sample glued to sample platform. Holes were machined into the stage body to accommodate inductive or capacitive sensors. The sensors are held in place with set screws as shown. **b** An AFM head [Nanosurf, easyScan 2 (www.nanoscience.com)] coupled with the positioning stage for high-speed AFM imaging experiments

The z-stage is designed using two 3×3 mm Noliac SCMAP06 piezo-stack actuators. The actuators are recessed within the nested x-stage. The base of each actuator is glued to an alumina plate while the free end is constrained using plate flexures. To increase the stiffness of the piezoactuators, the plate-stacks are used without the stock 1-mm thick ceramic insulating end-plates. Instead, the mounting face is insulated by the alumina base plate, while the top surface is insulated from the plate flexure with a thin sheet of mica. The experimental prototype is shown in Fig. 4.24 with the scanner body bolted to an aluminum base.

4.7.9 Drive Electronics

Due to the capacitive nature of piezoelectric transducers, high-speed operation requires large current and power dissipation. For example, the fast scanning axes, x and z, require drive electronics capable of supplying sufficient power to drive the capacitive piezoelectric loads at high frequency. If the maximum driving voltage, trajectory, and frequency are known, the current and power dissipation are easily computed by conservatively approximating the transducer as a purely capacitive load. For example, the current

$$I_p = CsV_p, \tag{4.53}$$

where s is the Laplace variable, and C and V_p are the transducer capacitance (380 nF) and load voltage, respectively. The power dissipation in a linear amplifier is

$$P_d = I_p(V_s - V_p), \tag{4.54}$$

where V_s is the supply voltage (200 V).

For the example design, the nominal capacitances for the x- and z-axis actuators are 380 and 100 nF, respectively. The piezo-amplifiers are built around the Power Amp Design (www.powerampdesign.net) PAD129 power op-amp, with a gain bandwidth product of 1 MHz. A 200 V DC power supply is constructed from two linear regulated 100 V, 3 A DC power supplies (Acopian A100HT300) connected in series. A 35 kHz low pass filter is used to smooth the input signal to the power op-amp. Commercially available high-bandwidth amplifiers are available from suppliers such as PiezoDrive, Australia; Trek Inc., Japan; and PiezoMechanik, Germany. A more detailed discussion of electrical considerations is presented in Chap. 14.

4.7.10 Experimental Results

The fabricated scanner shown in Fig. 4.24 is tested to determine the stiffness, maximum range, and dynamic characteristics. Prior to assembly, the effective stiffnesses of the x- and y-stage are determined by taking the ratio of the measured displacement due to an applied load. Static loads are applied to the stages by mounting the scanner vertically to a fixture (z-axis perpendicular to ground), running a cable through the hole in the x-stage and hanging masses from the cable. A total of 15 Lbf (66.7 N) is applied in the positive and negative direction in 2.5 Lbf (11.1 N) increments. Displacement is measured using a Kaman inductive sensor (SMU9000-15N). The analytical, FEA predicted, and measured stiffnesses are 7.82, 7.42, and 3.81 N/μm, respectively, for the x-stage and 4.28, 4.04, and 5.10 N/μm, respectively, for the y-stage. The discrepancy between the predicted and measured values are attributed to machining tolerances.

Application of 180 V peak-to-peak sine input at 10 Hz to the x and y piezoactuators resulted in 8.19 and 8.34 μm travel, respectively. Since the x and y axes can tolerate a maximum of 200 V, the maximum lateral range of the stage is approximately 9×9 μm. Application of 200 V peak-to-peak sine input at 10 Hz to the vertical z piezoactuators will give approximately 1 μm of travel. Over these ranges, the measured x/y cross coupling is 75 nm peak-to-peak (1.83 % or −34.75 dB) in y caused by actuating the x piezo and 24 nm peak-to-peak (0.6 % or −44.44 dB) in x caused by actuating the y piezo. The measured vertical runouts are 27.6 nm peak-to-peak (0.35 % or −49.2 dB) caused by actuating the x piezo and 81.4 nm peak-to-peak (0.97 % or −40.3 dB) caused by actuating the y piezo. It is noted that the lateral x-to-y and y-to-x cross coupling may be caused by the y-stage's compliance. For example, x-actuation may cause slight deformation in the y-stage body leading to measured cross coupling. Similarly, lateral-to-vertical cross coupling (x-to-z and y-to-z) may be caused by a tilted sample or misalignment of the displacement sensor, e.g., when the tilted sample translates laterally, the tilted surface may appear to move vertically relative to a fixed sensor.

Frequency response functions are measured using a dynamic signal analyzer (Stanford Research Systems SRT785). Small inputs (<70 mV) are applied to the piezo amplifiers during the test to minimize the effect of nonlinearity such as

hysteresis. Measurements for the x- and y-stages are taken with both the stage mounted sensors (inductive sensor for x, and ADE Capacitive sensor for y) and again with a single point laser vibrometer (Polytec CLV-1000 with CLV-800-vf40 laser unit) mounted to the vibration isolation table (for both x and y). The measured responses are shown in Fig. 4.21 along with the FEA predictions. When measured relative to the y-stage body, the x-stage has a dominant first resonance peak at 24.2 kHz (a2) which matches well with the predicted value of 25.9 kHz (a1). Several small pole/zero pairs appear before the dominant peak. However, when measured using a laser vibrometer relative to an outside body such as the vibration isolation table (a3), the response shows additional unexpected resonances. These peaks are thought to be due to modes in the y-stage being excited by the x-stage. Unfortunately, these modes are not detectable when the sensor is attached to the y-stage body. The measured dominant resonance for the y-stage at 6.0 kHz, both measured using the capacitive displacement sensor attached to the stage body (a2) and the laser vibrometer on table (a3) matches the predicted FEA value (a1) at 5.96 kHz very well. Not only do the dominant resonances agree with the FEA results, they are also piston modes relative to their mounting point as predicted by FEA. The frequency response for the z-axis is measured using the deflection of a 360 kHz tapping-mode AFM cantilever (Vista Probes T300 www.vistaprobes.com) in contact-mode over the sample surface. The dominant resonance is approximately 70 kHz in the actuation (piston) mode.

4.8 Chapter Summary

This chapter described the design considerations for high-speed nanopositioning. An example three-axis, serial-kinematic high-speed scanner based on piezo-stack actuators is used to illustrate the design process. Important considerations include:

- balancing the tradeoff between scanning range and achievable mechanical resonance,
- taking advantage of FEA tools to optimize mechanical resonances, and
- designing drive electronics which considers the capacitive nature of piezoactuators.

The example scanner achieved a range of approximately $9 \times 9 \times 1$ μm, where the fast scanning axis is optimized for speed. Experimental results showed a good correlation with simulation, where finite element analysis predicted the dominant resonances along the fast (x-axis) and slow (y-axis) scanning axes at 25.9 and 6.0 kHz, respectively. The measured dominant resonances of the prototype stage in the fast and slow scanning directions were measured at 24.2 and 6.0 kHz, respectively, which were in good agreement with the FEA predictions. In the z-direction, the measured dominant resonance was measured at approximately 70 kHz. This is sufficient to achieve SPM line rates in excess of 3 kHz.

References

Ando T, Kodera N, Uchihashi T, Miyagi A, Nakakita R, Yamashita H, Matada K (2005) High-speed atomic force microscopy for capturing dynamic behavior of protein molecules at work. E-J Surf Sci Nanotechnol 3:384–392

Ando T, Uchihashi T, Fukuma T (2008) High-speed atomic force microscopy for nano-visualization of dynamic biomolecular processes. Prog Surf Sci 83(7–9):337–437

Ando T, Kodera N, Maruyama D, Takai E, Saito K, Toda A (2002) A high-speed atomic force microscope for studying biological macromolecules in action. Jpn J Appl Phys Part 1. 41(7B): 4851–4856

Bechtold R, Rudnyi E, Korvink J (2005) Dynamic electro-thermal simulation of microsystems-a review. J Micromech Microeng 15(11):R17–R31

Beer FP, Johnston ER (1992) Mechanics of materials, 2nd edn. McGraw Hill, New York

Bell DJ, Lu TJ, Fleck NA, Spearing SM (2005) MEMS actuators and sensors: observations on their performance and selection for purpose. J Micromech Microeng 15(7):S153–S164

Clayton GM, Tien S, Leang KK, Zou Q, Devasia S (2009) A review of feedforward control approaches in nanopositioning for high-speed SPM. J Dyn Syst Meas Contr 131:061 101(1–19)

Craig RR (2000) Mechanics of materials, 2nd edn. John Wiley & Sons, New York

Damjanovic D, Newnham RE (1992) Electrostrictive and piezoelectric materials for actuator applications. J Intell Mater Syst Struct 3(2):190–208

Devos S, Reynaerts D, Brussel HV (2008) Minimising heat dissipation in ultrasonic piezomotors by working in a resonant mode. Precis Eng 32:114–125

Fleming AJ (2009) High-speed vertical positioning for contact-mode atomic force microscopy. In: Proceedings of IEEE/ASME international conference on advanced intelligent mechatronics, Singapore, pp 522–527

Geisberger A, Sarkar N (2006) MEMS/NEMS: techniques in microelectrothermal actuator and their applications. Springer, New York

Guthold M, Zhu X, Rivetti C, Yang G, Thomson NH, Kasas S, Hansma HG, Smith B, Hansma PK, Bustamante C (1999) Real-time imaging of one-dimensional diffusion and transcription by escherichia coli rna polymerase. Biophys J 77(4):2284–2294

Hicks TR, Atherton PD, Xu Y, McConnell M (1997) The nanopositioning book. Queensgate Intstruments Ltd., Berkshire

Howell LL (2001) Compliant mechanisms. John Wiley & Sons, New York

Hubbard NB, Culpepper ML, Howell LL (2006) Actuators for micropositioners and nanopositioners. Appl Mech Rev 59(6):324–334

Humphris ADL, Hobbs JK, Miles MJ (2003) Ultrahigh-speed scanning near-field optical microscopy capable of over 100 frames per second. Appl Phys Lett 83(1):6–8

Inman D (2001) Engineering vibration, 2nd edn. Prentice Hall, Upper Saddle River

Kenton BJ (2010) Design, characterization, and control of a high-bandwidth serial-kinematic nanopositioning stage for scanning probe microscopy applications. Ph.D. dissertation, Mechanical Engineering

Kenton BJ, Leang KK (2012) Design and control of a three-axis serial-kinematic high-bandwidth nanopositioner. IEEE/ASME Trans Mech 17(2):356–369

Kindt JH, Fantner GE, Cutroni JA, Hansma PK (2004) Rigid design of fast scanning probe microscopes using finite element analysis. Ultramicroscopy 100(3–4):259–265

Leang KK, Fleming AJ (2009) High-speed serial-kinematic AFM scanner: design and drive considerations. Asian J Control Spec Issue Adv Control Methods Scan Probe Microsc Res Tech 11(2):144–153

Liu C (2006) Foundations of MEMS. Prentice Hall, Upper Saddle River

Lobontiu N (2003) Compliant mechanisms design of flexure hinges. CRC Press LLC, Boca Raton

Muller K-D, Marth H, Pertsch P, Stiebel C, Zhao X (2007) Piezo based long travel actuators in special environmental conditions. In: 12th European space mechanisms and tribology symposium (ESMATS), pp SP–653

Park SR (2005) A mathematical approach for analyzing ultra precision positioning system with compliant mechanism. J Mater Res Process Technol 164–165:1584–1589
Physik Instrumente (2009) Piezo nano positionoing: Inspirations 2009
Picco LM, Bozec L, Ulcinas A, Engledew DJ, Antognozzi M, Horton M, Miles MJ (2007) Breaking the speed limit with atomic force microscopy. Nanotechnology 18(4):044 030(1–4)
Rifai OME, Youcef-Toumi K (2001) Coupling in piezoelectric tube scanners used in scanning probe microscopes. In: American Control Conference, vol 4, pp 3251–3255
Rost MJ, Crama L, Schakel P, van Tol E, van Velzen-Williams GBEM, Overgauw CF, ter Horst H, Dekker H, Okhuijsen B, Seynen M, Vijftigschild A, Han P, Katan AJ, Schoots K, Schumm R, van Loo W, Oosterkamp TH, Frenken JWM (2005) Scanning probe microscopes go video rate and beyond. Rev Sci Instrum 76(5):053 710–1–053 710–9
Sahu B, Taylor CR, Leang KK (2010) Emerging challenges of microactuators for nanoscale positioning, assembly, and manipulation", ASME J Manuf Sci Eng Special Issue Nanomanuf 132(3):030917 (16 pages)
Samara-Ratna P, Atkinson H, Stevenson T, Hainsworth SV, Sykes J (2007) Design of a micromanipulation system for high temperature operation in an environmental scanning electron microscope (ESEM). J Micromech Microeng 17(1):104–114
Schilfgaarde MV, Abrikosov IA, Johansson B (1999) Origin of the Invar effect in iron-nickel alloys. Nature 400(6739):46–49
Schitter G (2007) Advanced mechanical design and control methods for atomic force microscopy in real-time. In: American Control Conference, 2007, pp 3503–3508
Schitter G, Stemmer A (2004) Identification and open-loop tracking control of a piezoelectric tube scanner for high-speed scanning-probe microscopy. IEEE Trans Control Syst Technol 12(3): 449–454
Schitter G, Rost MJ (2008) Scanning probe microscopy at video-rate. Mater Today 11(1):40–48
Schitter G, Thurner PJ, Hansma PK (2008) Design and input-shaping control of a novel scanner for high-speed atomic force microscopy. Mechatronics 18(5–6):282–288
Schitter G, Åström KJ, DeMartini BE, Thurner PJ, Turner KL, Hansma PK (2007) Design and modeling of a high-speed AFM-scanner. IEEE Trans Control Syst Technol 15(5):906–915
Schitter G, Rijkee WF, Phan N (2008) Dual actuation for highbandwidth nanopositioning. In: IEEE conference on decision and control, 2008, pp 5176–5181
Scire FE, Teague EC (1978) Piezodriven 50-μm range stage with subnanometer resolution. Rev Sci Instr 49(12):1735–1740
Smith T (2000) Flexures: elements of elastic mechanisms. Gordon and Breach, Amsterdan
Snow ES, Campbell PM, Perkins FK (1997) Nanofabrication with proximal probes. Proc IEEE 85(4):601–611
Stillesjo F, Engdahl G, Bergqvist A (1998) A design technique for magnetostrictive actuators with laminated active material. IEEE Trans Magn 34(4):2141–2143
Tan X, Baras JS (2004) Modeling and control of hysteresis in magnetostrictive actuators. Automatica 40:1469–1480
Timoshenko SP (1953) History of strength of materials. McGraw-Hill Book Company, New York
Tsodikov SF, Rakhovsky VI (1998) Magnetostrictive force actuators for superprecise positioning. In: International symposium on discharges and electrical insulation in vacuum (ISDEIV), vol 2, pp 713–719
Waram T (1993) Actuator design using shape memory alloys, 2nd edn. T. C. Waram, Ontario
Yong YK, Aphale SS, Moheimani SOR (2009) Design, identification, and control of a flexure-based xy stage for fast nanoscale positioning. IEEE Trans Nanotechnol 8(1):46–54
Yong Y, Moheimani SOR, Kenton BJ, Leang KK (2012) Invited review: high-speed flexure-guided nanopositioning: mechanical design and control issues. Rev Sci Instrum 83(12):121101
Young WC, Budynas RG (2002) Roark's formula for stress and strain, 7th edn. McGraw-Hill, New York